LITHOS 436–437 (2023) 106951

Contents lists available at ScienceDirect

LITHOS

journal homepage: www.elsevier.com/locate/lithos

Evidence for early Pennsylvanian subduction initiation in the Mongol–Okhotsk Ocean from the Adaatsag ophiolite (Mongolia)

Mingshuai Zhu [a,b,*], Daniel Pastor-Galán [c,d], Laicheng Miao [a,b], Fuqin Zhang [a,b], Ariuntsetseg Ganbat [e], Shun Li [f], Shunhu Yang [a,b], Zeli Wang [g]

[a] Key Laboratory of Mineral Resources, Institute of Geology and Geophysics, Chinese Academy of Sciences, Beijing 100029, China
[b] Institutions of Earth Science, Chinese Academy of Sciences, Beijing 100029, China
[c] Department of Geodynamics, Universidad de Granada, Campus Fuentenueva, 18071 Granada, Spain
[d] Frontier Research Institute for Interdisciplinary Sciences, Tohoku University, Japan
[e] Department of Earth Sciences, The University of Hong Kong, Hong Kong Special Administrative Region, China
[f] School of Oceanography, Shanghai Jiao Tong University, Shanghai 200030, China
[g] Shandong Key Laboratory of Depositional Mineralization and Sedimentary Minerals, Shandong University of Science and Technology, Qingdao 266590, China

ARTICLE INFO

Keywords:
Subduction initiation
Adaatsag ophiolite
Mongol–Okhotsk Ocean
Forearc basalts
High-Mg diorite

ABSTRACT

The Late Paleozoic–Mesozoic Mongol–Okhotsk Ocean was the latest ocean basin witnessing the final amalgamation of East Asia. However, the kinematic evolution and geodynamics of Mongol–Okhotsk's subduction initiation remain enigmatic mainly due to the lack of appropriate studies of its ophiolitic records. Here, we report for the first time a subduction initiation record from the Adaatsag ophiolite in the central Mongolia. This ophiolite presents a magmatic sequence akin to that in the Izu–Bonin–Mariana forearc, considered archetypical of subduction initiation. The gabbroic and basaltic rocks of the ophiolite display geochemical signatures similar to the forearc basalts. Zircon U—Pb geochronology of the gabbro shows a mean age of 319 ± 2 Ma, which we interpret as crystallization age. The high-Mg diorite intruding the gabbros of the ophiolite displays a transitional affinity between sanukite and boninite. Zircon U—Pb geochronology of the high-Mg diorite shows a mean age of 317 ± 2 Ma. Together with the neighbor Khuhu Davaa suprasubduction zone ophiolite (~321 Ma), we interpret that the subduction of the southwestern Mongol–Okhotsk Ocean initiated during the Early Pennsylvanian (~320 Ma). The structurally underlying gneissic granite (~534 Ma) indicates the Adaatsag ophiolite was emplaced southward onto the Ereendavaa cratonic terrane, and the overlying molassic sequences (youngest detrital zircon peak age of ~252 Ma) constrain this emplacement occurred before ~252 Ma. The older (499–870 Ma) inherited zircons of the ophiolites and negative Hf isotope data of the high-Mg diorite indicate that a continental fragment existed in the newly formed intra-oceanic arc, which probably facilitated the Early Pennsylvanian subduction initiation in the Mongol–Okhotsk Ocean.

1. Introduction

Subduction is regarded as the main driving force of plate tectonics (Arculus et al., 2015; Guilmette et al., 2018; Stern, 2004) and so far, the Earth is the only known planet where subduction occurs. We have not observed directly any place where subduction is initiating at any of the numerous subducting segments at present. Such lack of information makes the mechanisms and kinematics responsible for subduction initiation hypothetical and heavily disputed (Crameri et al., 2020; Stern, 2004; Stern and Gerya, 2018; van Hinsbergen et al., 2015). Subduction initiation, either induced or spontaneous, probably occurs predominantly within pre-existing or imposed lithospheric weaknesses (Guilmette et al., 2018; Stern and Gerya, 2018). The Izu-Bonin-Mariana (IBM) oceanic arc is likely the best-preserved record of subduction initiation and subsequent oceanic arc evolution. There, the generation of earliest MORB-like forearc basalts (FABs) during subduction initiation was followed by eruption of boninites and other high-Mg andesites (HMAs), and finally arc tholeiites and calc-alkaline rocks (e.g., Hickey-Vargas et al., 2018; Reagan et al., 2010). Ophiolites are direct evidence of ancient ocean subduction. In particular, supra-subduction zone (SSZ) ophiolites are thought to represent on-land fragments of the forearc oceanic crust documenting subduction initiation events (e.g., Whattam

* Corresponding author at: Key Laboratory of Mineral Resources, Institute of Geology and Geophysics, Chinese Academy of Sciences, Beijing 100029, China.
E-mail address: zhumingshuai@mail.iggcas.ac.cn (M. Zhu).

https://doi.org/10.1016/j.lithos.2022.106951
Received 31 July 2022; Received in revised form 6 November 2022; Accepted 18 November 2022
Available online 24 November 2022

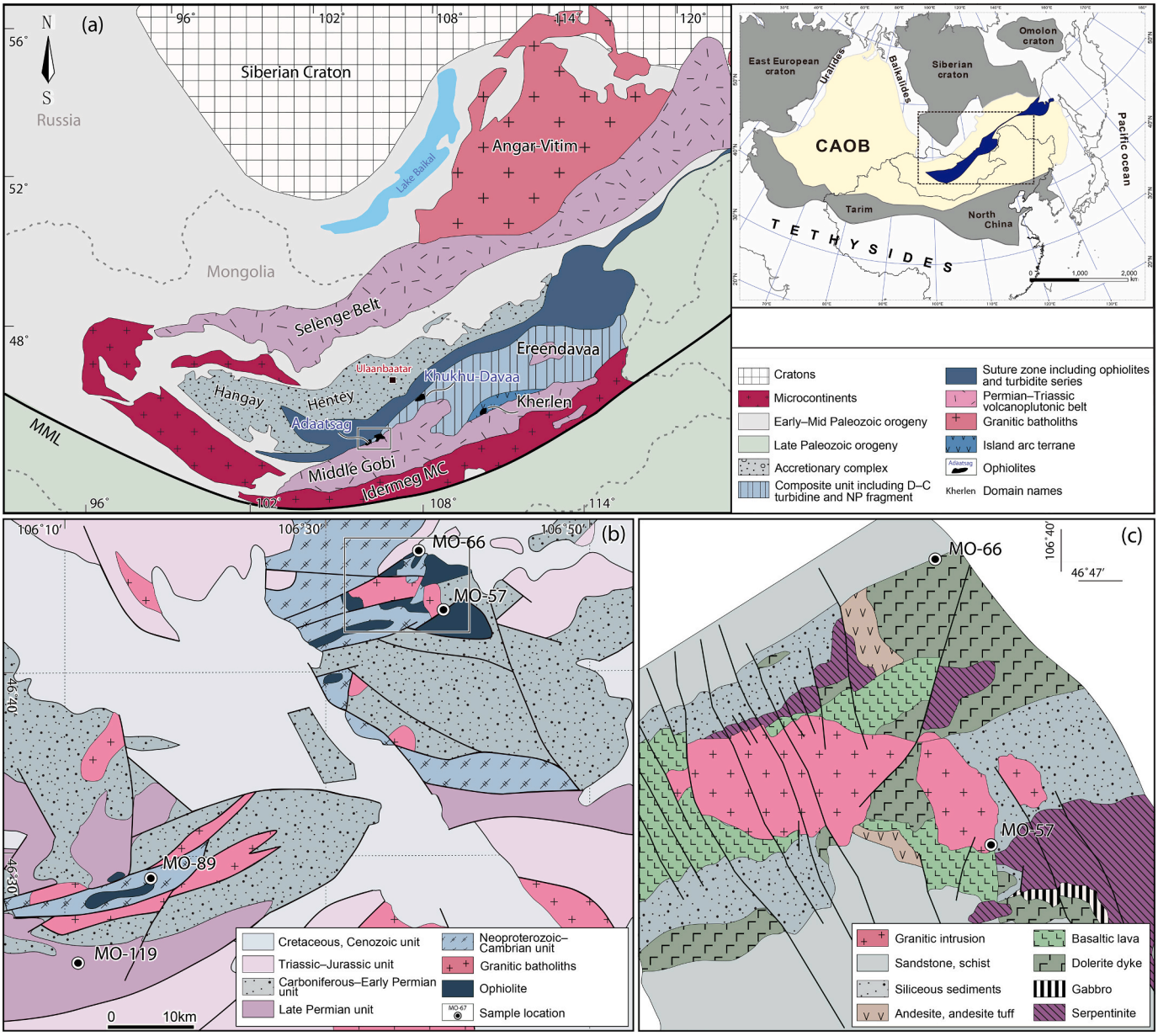

Fig. 1. (a) Tectonic map showing the main tectonic units of the Mongol–Okhotsk orogenic belt (modified from Bussien et al., 2011). (b, c) Geologic map of the Adaatsag ophiolite study area. MML- Main Mongolian Lineament.

and Stern, 2011). Especially, the comparison between ophiolite chemostratigraphy (variations in lava chemistry through time) with that of the IBM forearc can provide important constraints on the subduction initiation of oceans in ancient orogens (e.g., Li et al., 2020; Ren et al., 2014).

The Central Asian Orogenic Belt (CAOB) is possibly the largest accretionary orogen worldwide, which formed through multiple convergence and collision events of various components driven by the closure of the Paleo-Asian Ocean (e.g., Windley et al., 2007; Xiao et al., 2015). The Mongol–Okhotsk belt (MOB) is the youngest segment of the CAOB and extends from central Mongolia in northeastern direction to the Uda Gulf in the Okhotsk Sea (e.g., Bussien et al., 2011; Zorin, 1999) (Fig. 1a). The MOB formation is linked to the evolution of the Late Paleozoic–Mesozoic Mongol–Okhotsk Ocean (MOO) between the Siberian Craton and the Amur Block, which was an embayment of the Paleo-Pacific during the Pangea assembly (e.g., Donskaya et al., 2013; Zorin, 1999). The final closure of the MOO is estimated to have occurred between the Early–Middle Jurassic and Early Cretaceous witnessing the final amalgamation of East Asia (e.g., Sorokin et al., 2020; Van der Voo et al., 2015; Yi and Meert, 2020). Thus, the tectonic evolution of East Asia was dominated by the Paleo-Asian Ocean during the Paleozoic superimposed by the younger MOO (e.g., Wu et al., 2011; Zhao et al., 2019). However, the switch of these two tectonic regimes, which controls the spatial and temporal distribution of the magmatic records, remains underexplored partially because the timing and mechanism of subduction initiation in the MOO is not well constrained.

In this study, we report a newly identified intra-oceanic magmatic record including FABs and high-Mg diorite in the Adaatsag ophiolite, the southwestern segment of the Mongol–Okhotsk suture zone. Our geochronological and geochemical data provide key evidence for a progressively evolving intra-oceanic arc system with continental basement, and Early Pennsylvanian subduction initiation in the southwest segment of the MOO.

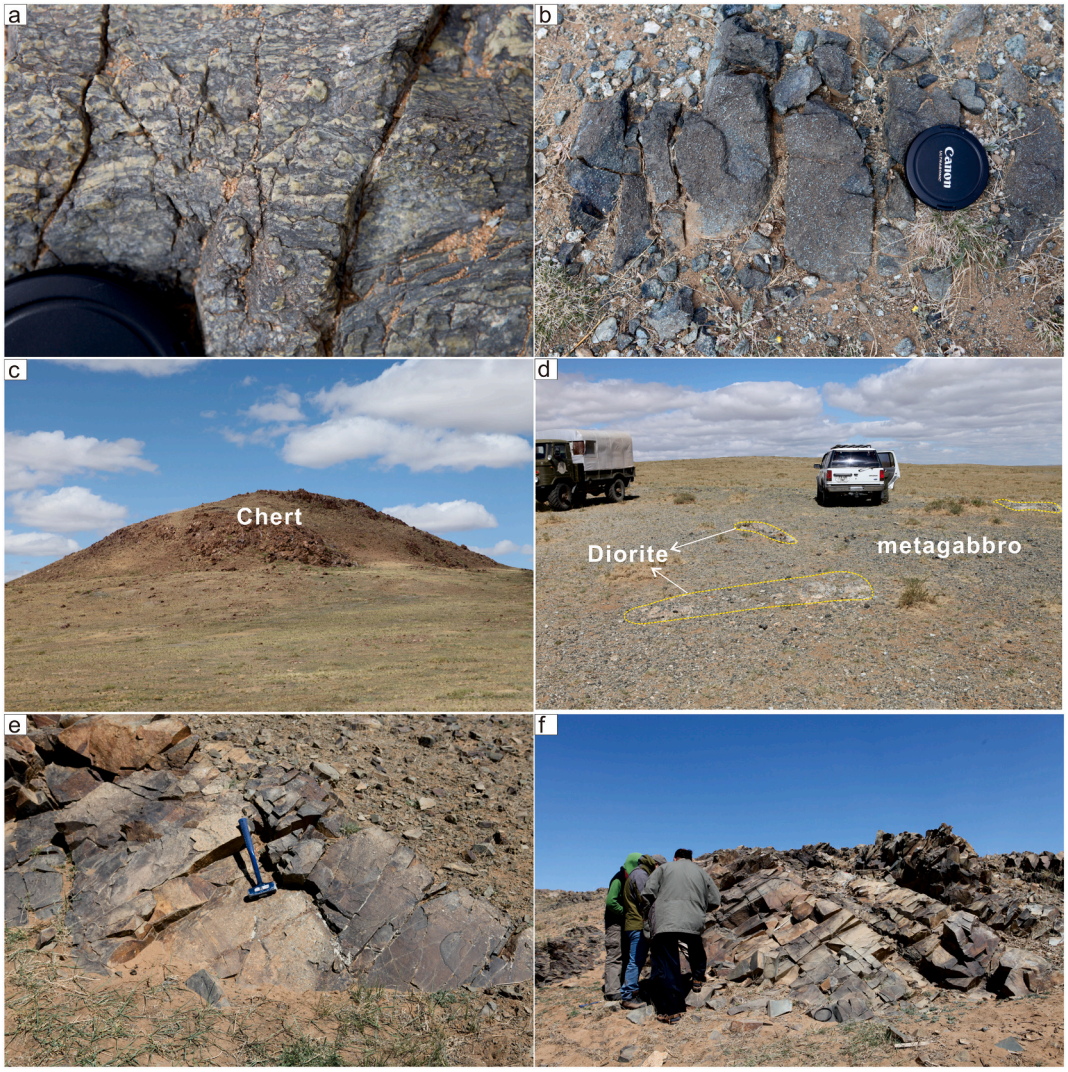

Fig. 2. Field photographs showing the occurrences of the Adaatsag ophiolite and overlying late Permian Horinj Formation. (a) Serpentinized ultramafic rocks; (b) Gabbro; (c) Red chert on top of the basalts; (d) Diorite intruding the metagabbro of the ophiolite; (e) Conglomerate layer of the Horinj Formation; (f) Sandstone layers of the Horinj Formation. (For interpretation of the references to colour in this figure legend, the reader is referred to the web version of this article.)

2. Geological background

Mongolia has been traditionally divided into two tectonic domains separated by the Main Mongolian Lineament (Fig. 1a), namely an Early Paleozoic domain to the north and a Late Paleozoic domain to the south (Badarch et al., 2002; Windley et al., 2007). The northern domain is composed of the Archean–Proterozoic microcontinents, Neoproterozoic to Lower Paleozoic metamorphic rocks and ophiolites, and Paleozoic volcanic and sedimentary rocks, while the southern domain mainly consists of Lower to Middle Paleozoic ophiolites and arc-related volcanic and volcaniclastic rocks (e.g., Badarch et al., 2002). The northern domain is crosscut by the younger MOB, which is related to the subduction and closure of the MOO (Bussien et al., 2011; Donskaya et al., 2013) (Fig. 1a).

The Hangay–Hentey belt (Fig. 1a) is mainly composed of the Silurian to Carboniferous turbidites, which were unconformably overlain by Triassic continental deposits (Badarch et al., 2002; Bussien et al., 2011). Specifically, the Silurian–Devonian formations mainly consist of pelagic red radiolarian chert beds, and deep-sea turbidite deposits with OIB-type mafic volcanic rocks. Whereas, the Carboniferous series shows a shallowing-upward trend from turbidites to proximal delta deposits (Bussien et al., 2011; Kelty et al., 2008; Kurihara et al., 2009). Detrital zircon geochronological studies showed age distributions peaking in the Mississippian (Kelty et al., 2008) or/and the Devonian (Bussien et al., 2011). This belt has been interpreted as a Devonian–Carboniferous accretionary wedge at the northern margin of the MOO (Bussien et al., 2011; Kurihara et al., 2009).

The Middle Gobi volcano-plutonic belt mainly comprises Permian–Triassic calc-alkaline andesites, dacites, rhyolites, trachyrhyolites and granites, which document the southward subduction of the MOO (e.g., Tomurtogoo et al., 2005; Zhao et al., 2017). According to the terrane division of Badarch et al. (2002), the basement of this magmatic belt is the Ereendavaa terrane, which is defined as a cratonic terrane with a Paleoproterozoic basement overlain by Neoproterozoic metasedimentary and volcanic rocks. However, recent age dating results suggest that the putative Precambrian gneiss, amphibolite, and schist of the Ereendavaa terrane formed, in fact, during the Early–Middle Paleozoic (512–419 Ma), perhaps from the evolution of the Kherlen Ocean evidenced by the Kherlen ophiolite (ca. 566–510 Ma) (Miao et al., 2016, 2017; Narantsetseg et al., 2019). Occurrence of ~440 Ma post-collisional granites indicate that the Kherlen Ocean had closed by the Silurian leading to the amalgamation of the Ereendavaa and Idermeg continental terranes (Miao et al., 2016), which together constitute the southern continental margin of the MOO.

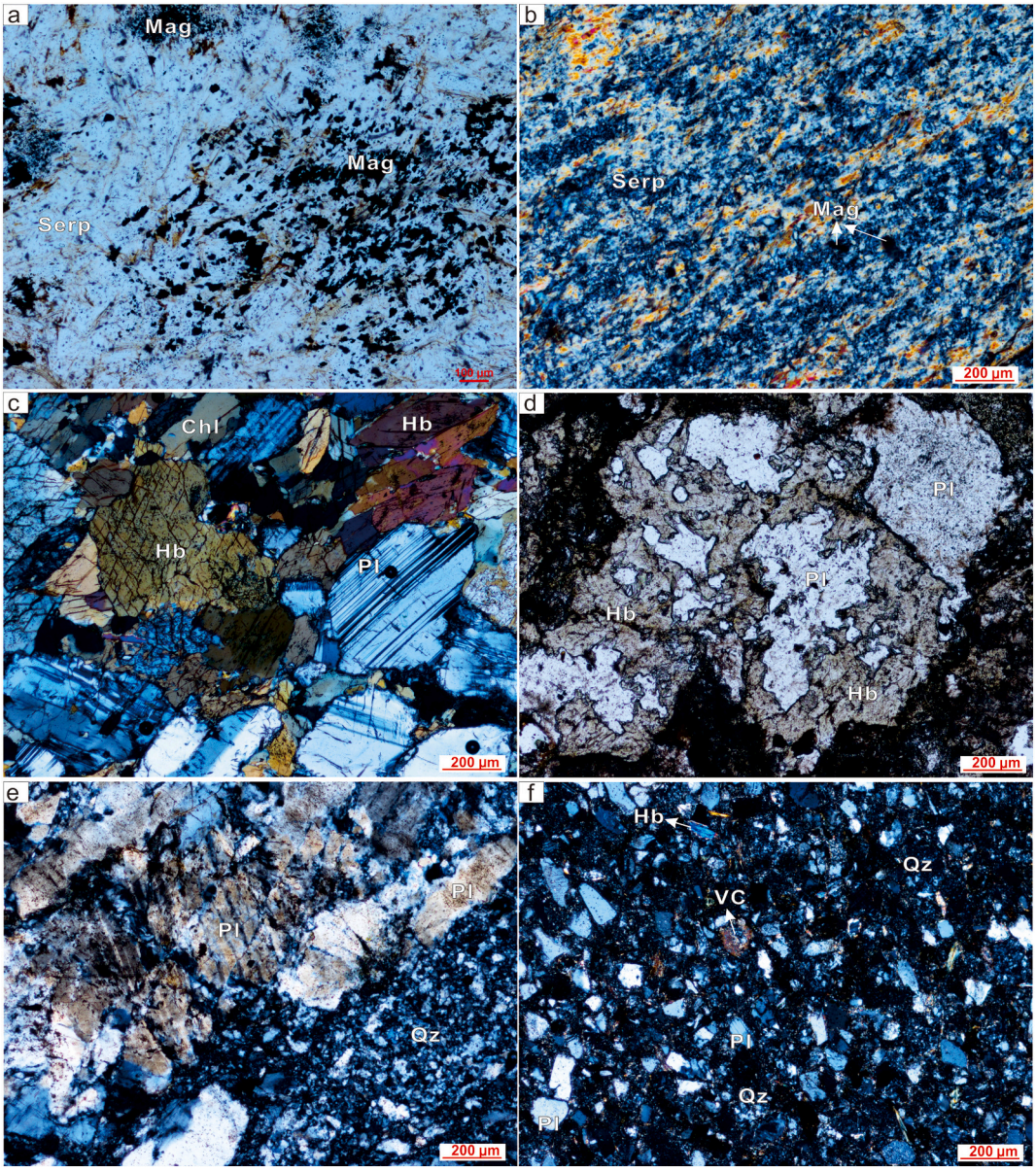

Fig. 3. Microphotographs of the Adaatsag ophiolite and the samples for age dating. (a, b) Ultramafic rocks with strong serpentinization; (c) Metagabbro with a poikilitic texture; (d) High-Mg quartz diorite intruding the metagabbro; (e) Gneissic granite on which the Adaatsag ophiolite was thrust; (f) Sandstone sample from the Horinj Formation. Abbreviations: Serp, serpentine; Mag, magnetite; Hb, hornblende; Chl, chlorite; Pl, plagioclase; Qz, quartz; VC, Volcaniclastics.

Herein, we have studied ophiolitic rocks from the Adaatsag suture zone, which is bordered by the Hangay-Hentey belt to the northwest and the Middle Gobi volcano-plutonic belt to the southeast (Badarch et al., 2002) (Fig. 1a). The Adaatsag suture zone mainly consists of quartzite, metasandstone, chert, metavolcanic rocks, limestone, and fragments of ophiolite, which are highly deformed and underwent greenschist to amphibolite facies metamorphism (Badarch et al., 2002; Tomurtogoo et al., 2005; Zhu et al., 2018). As the northeastern continuation of the Adaatsag suture zone, the Dochgol terrane contains deformed and metamorphosed Devonian to Triassic marine sandstone, shale, conglomerate, and minor volcanic rocks (Badarch et al., 2002; Bussien et al., 2011).

3. Geology and petrography of the Adaatsag ophiolite

The Adaatsag ophiolite lies at the southwestern end of the Adaatsag suture zone, about 200 km Southwest of Ulaanbaatar, Mongolia (Fig. 1a, b). The ophiolite comprises serpentinized and carbonated dunite and harzburgite, clinopyroxenite, layered gabbro, isotropic gabbro, sheeted dykes, and basaltic lavas from bottom to top. They are overlain by chert and siliceous sandstone (Fig. 1c and Fig. 2a, b, c). Some leucogabbro pegmatite dykes occur within the layered gabbro, which yielded a single-zircon evaporation age of ca. 325 Ma (Tomurtogoo et al., 2005). Locally, quartz diorite and plagiogranite dykes intruded the isotropic gabbro (Fig. 2d). The Carboniferous–Early Permian strata intercalated with the ophiolite mainly comprise sandstones, siltstones, andesite and volcaniclastic rocks (Fig. 1b). The Late Permian strata unconformably overlying or in fault contact with the ophiolite are composed of non-marine conglomerate, conglomeratic sandstone and medium to coarse-grained sandstone (Horinj Formation), which have been subjected to some deformation (Fig. 2e, f). The unit structurally underlying the ophiolite is the Neoproterozoic–Cambrian North Gobi Formation, which mainly consists of muscovite schist, quartz-amphibolite, biotite-amphibolite, and gneissic granite (Fig. 1b).

The peridotites are extensively serpentinized, and olivine and orthopyroxene are completely or partly replaced by serpentine (Fig. 3a,

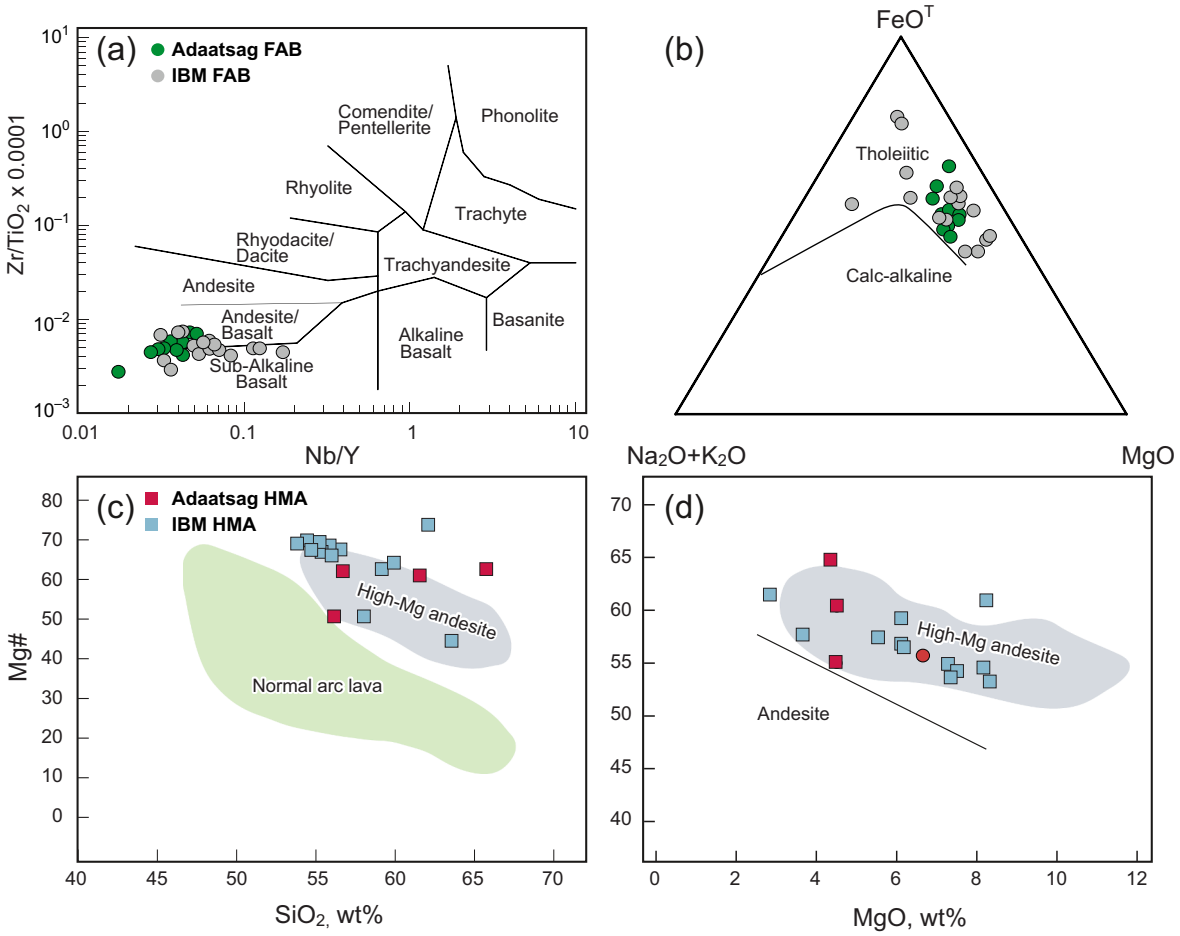

Fig. 4. Discrimination diagrams of the basalt and high-Mg diorite of the Adaatsag ophiolite. (a) Plots of Nb/Y vs. Zr/(TiO_2 * 0.0001) (Winchester and Floyd, 1977). (b) FeO*-Na_2O + K_2O-MgO diagram (Irvine and Baragar, 1971). (c) Plots of SiO_2 vs MgO (McCarron and Smellie, 1998). (b) Plots of Mg# vs SiO_2 (McCarron and Smellie, 1998). Data sources of IBM forearc basalts and high-Mg andesites are from Reagan et al. (2010) and Shervais et al. (2021), respectively.

b). Peridotite contains 70–80% (modal volume percentage) serpentine, 15% magnetite, ~5% olivine, and ~ 5% orthopyroxene. The gabbro is medium- to coarse-grained and has a poikilitic texture (Fig. 3c). It consists mainly of hornblende (~40%), plagioclase (~50%) and pyroxene (~10%). Some mafic minerals (hornblende and pyroxene) have been altered to chlorite. Locally, the plagioclase phenocrysts contain some hornblende and pyroxene inclusions. The quartz diorite intruding the isotropic gabbro consists mainly of plagioclase (35–45 vol%), quartz (10–15 vol%), and amphibole (30–40 vol%) (Fig. 3d). Quartz often occurs as an anhedral grain filled in the lacuna of the subhedral plagioclase and amphibole. The gneissic granite from the North Gobi Formation exhibits a porphyritic-like texture. The plagioclase porphyroblasts (~60%) are commonly subhedral–euhedral (0.6–1.2 mm), while quartz is commonly anhedral (<0.2 mm) (Fig. 3e). The analyzed Late Permian sandstone is mainly composed of feldspar (~55%), quartz (30%), mafic minerals (~5%, mainly hornblende and chlorite) and rock fragments (~10%, mainly igneous type) (Fig. 3f).

4. Analytical methods

4.1. Geochemistry

Whole-rock major and trace element compositions were determined at the Wuhan Sample Solution Analytical Technology Co., Ltd., China by X-ray fluorescence (XRF) and inductively coupled plasma mass spectrometry (ICP-MS). The precision of the XRF analyses is within ±2% for the oxides >0.5 wt% and within ±5% for the oxides >0.1 wt%. Analytical results for USGS standards indicated that the data are accurate within ±5% for the trace elements.

4.2. Zircon U—Pb geochronology

Zircon crystals were extracted from crushed rocks using conventional heavy liquid and magnetic separation techniques and hand-picked under a binocular microscope. The zircons were mounted in epoxy resin and polished to expose the grain centers. Optical (transmitted and reflected light) photographs and cathodoluminescence (CL) images were prepared to reveal the internal texture of the zircons in order to select optimal sites for analysis. Finally, the mounts were vacuum-coated with high-purity gold.

SIMS zircon U—Pb analyses were conducted using a CAMECA IMS-1280 ion microprobe at the Institute of Geology and Geophysics, Chinese Academy of Sciences following the procedures described by Li et al. (2010). U-Th-Pb ratios and absolute abundance were determined relative to the zircon standard 91,500 (Wiedenbeck et al., 1995). Isotopic compositions were corrected for common Pb using the measured ^{204}Pb concentrations. Corrections were sufficiently small to be insensitive to the choice of the common Pb isotopic composition. Therefore, an average of present-day crustal composition (Stacey and Kramers, 1975) was used, assuming that common Pb is largely surface contamination or from the gold coating introduced during sample preparation. Uncertainties of individual analyses are reported at the 1σ level; mean ages for pooled U/Pb analyses are given at the 95% confidence interval. Data reduction was performed using Isoplot 3.0 (Ludwig, 2003).

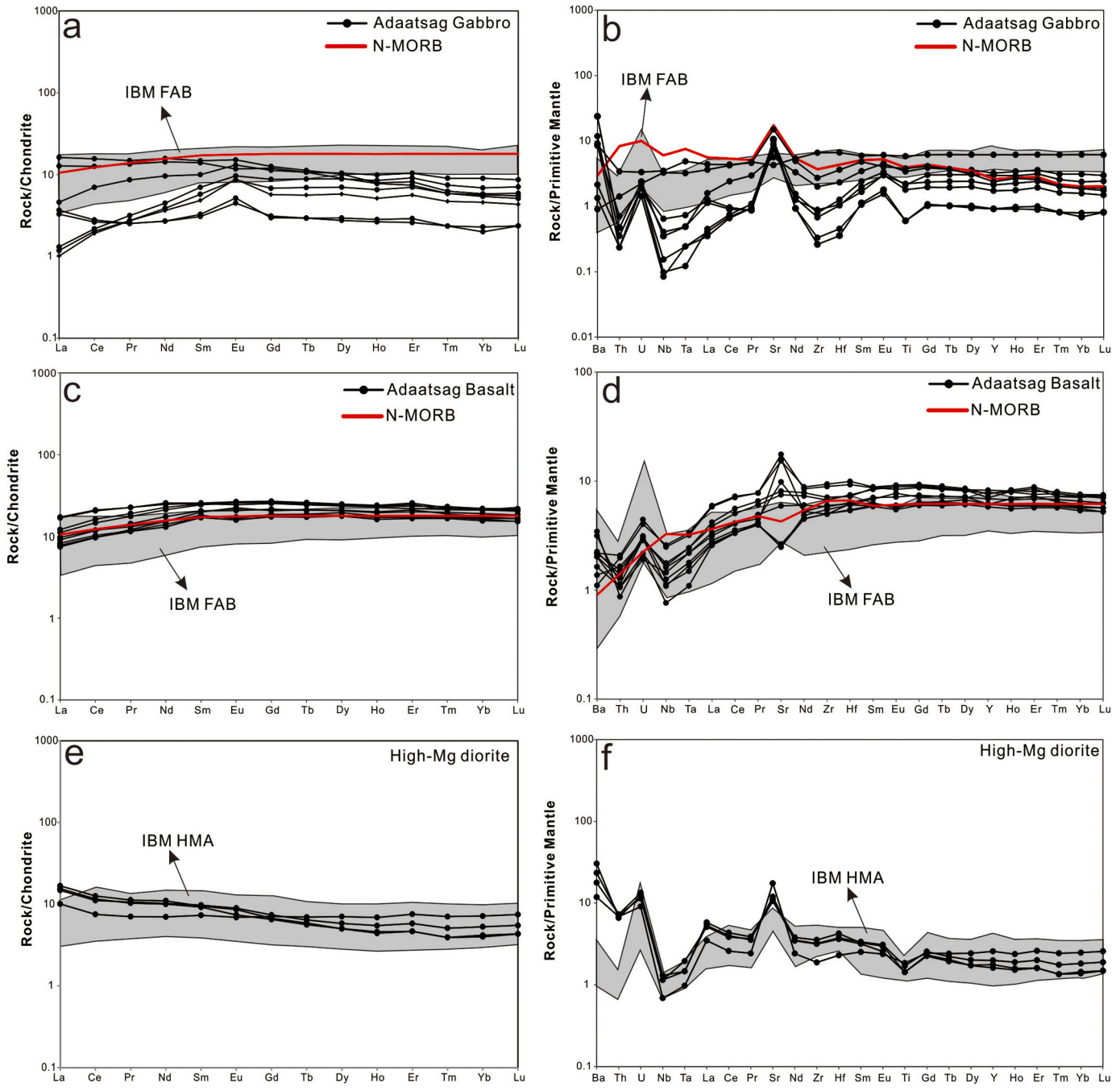

Fig. 5. Chondrite-normalized REE patterns and primitive-mantle normalized diagrams for the Adaatsag ophiolite. (a, b) Gabbros. (c, d) Basalts. (e, f) High-Mg diorites. Normalizing values are from Sun and McDonough (1989). Data sources of IBM forearc basalts and high-Mg andesites are from Reagan et al. (2010) and Shervais et al. (2021), respectively.

Zircon U—Pb dating by laser ablation inductively coupled plasma mass spectrometry (LA-ICP-MS) was conducted at Beijing GeoAnalysis CO., LTD. Pre-ablation was conducted for each spot analysis using 5 laser shots to remove potential surface contamination. The analysis was performed using a 30 μm diameter spot. The Iolite software package was used for data reduction (Paton et al., 2010). Zircon 91,500 was used as the primary reference material, whereas zircon GJ-1 (609 Ma; Jackson et al., 2004) and Plešovice (337 Ma; Sláma et al., 2008) were used to check accuracy. Typically, 35–40 s of the sample signals were acquired after 20 s of gas background measurement. The exponential function was used to calibrate the downhole fractionation (Paton et al., 2010). The analyses yielded weighted mean $^{206}Pb/^{238}U$ ages of 606 ± 5 Ma for GJ-1 and 338 ± 2 Ma for Plešovice, which agree with the reference values.

4.3. Zircon Hf analysis

In situ zircon Lu—Hf isotopes were carried out by the ICP-MC-MS at the Beijing Createch Testing Technology Co. Ltd. The laser ablation beam spot is 40 μm in diameter, and the analyzed pulse frequency of the laser beam is 8 Hz. Detailed analytical procedures are described in Wu et al. (2006). In the calculation of the εHf(t) values, the $^{176}Hf/^{177}Hf$ and $^{176}Lu/^{177}Hf$ ratios of present-day chondrite and the depleted mantle were (0.0332, 0.282772) and (0.0384, 0.28325), respectively (Griffin et al., 2000). The two-stage Hf model ages (T_{DM2}) were calculated by adopting $^{176}Lu/^{177}Hf = 0.015$ for the average continental crust (Griffin

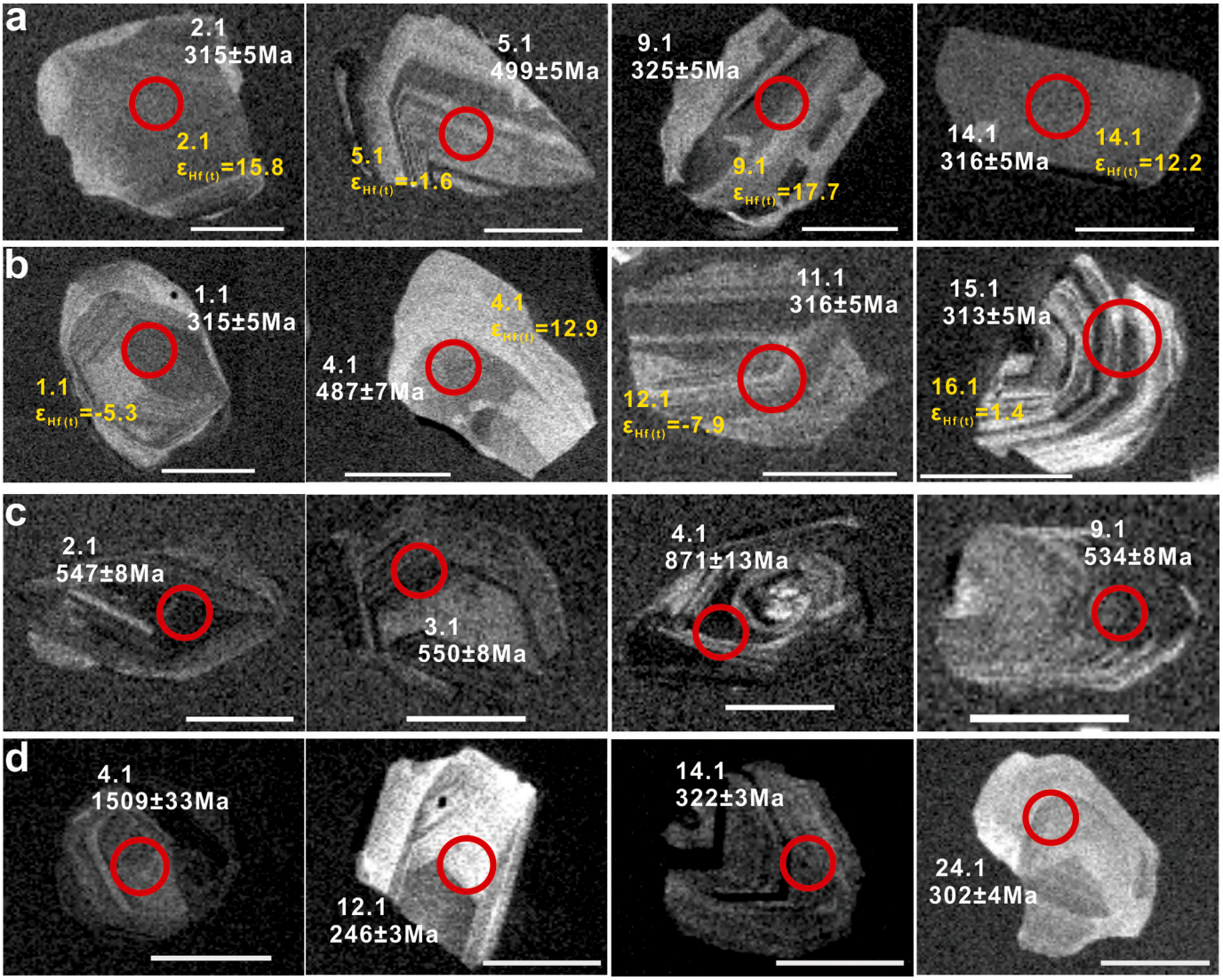

Fig. 6. Representative CL images of zircons from (a) Gabbro of the Adaatsag ophiolite (sample MO-66), (b) High-Mg diorite (sample MO-57), (c) Gneissic granite (sample MO-89) underlying the Adaatsag ophiolite, and (d) Sandstone of the Horinj Formation (sample MO-119). Red circles represent sites of analytical spots, and the numbers around the circles are the spot numbers and ages/$\varepsilon_{Hf\ (t)}$. (For interpretation of the references to colour in this figure legend, the reader is referred to the web version of this article.)

et al., 2004). The $^{176}Hf/^{177}Hf$ value of the standard zircon Plešovice tested in this experiment was 0.282480 ± 0.000016 (2σ), which is consistent with the value of the predecessor (Sláma et al., 2008) within the error range.

5. Results

5.1. Major and trace elements

Major and trace element compositions of the analyzed samples (four ultramafic samples, eight gabbro samples, ten basalt samples and four high-Mg diorite samples) from the Adaatsag ophiolite are presented in Table S1. Although fresh samples were carefully selected, the ultramafic rocks have high loss on ignition values (11.38–12.59 wt%), indicating variable degrees of alteration. The ultramafic rocks are characterized by low SiO_2 (38.56–40.40 wt%) and alkalinity ($Na_2O + K_2O$) contents (0.04–0.06 wt%), and high MgO (36.82–38.19 wt%) and $Fe_2O_3^T$ contents (7.97–11.06 wt%), with $Mg^{\#}$ [= molar Mg/(Mg + Fe^{2+})] ranging from 0.89 to 0.92. All samples have low total rare earth element (REE) contents (0.60–0.97 ppm), and the incompatible mantle trace elements such as Rb, Nb, Ta, and REE are strongly depleted (<0.1 ppm). In contrast, concentrations of mantle compatible elements such as Cr and Ni are extremely high in the samples (3127–4484 ppm for Cr and 1456–2732 ppm for Ni).

The gabbro samples exhibit variable SiO_2 (45.60–48.17 wt%), MgO (6.56–12.94 wt%), CaO (9.42–12.14 wt%), and Al_2O_3 (11.54–22.01 wt %) contents, but low Na_2O (0.83–1.91 wt%), TiO_2 (0.13–0.85 wt%), and P_2O_5 (0.01–0.07 wt%) contents. $Mg^{\#}$ values range from 0.69 to 0.86. The samples have REE contents between 7.15 and 33.99 ppm with no or positive Eu anomalies (Eu/Eu* =0.91–1.68). Four samples exhibit distinct chondrite-normalized light REE (LREE) depletion (La_N/Yb_N = 0.19–0.51), and four samples display LREE enrichment (La_N/Yb_N = 1.60–2.78) (Fig. 5a). In a primitive-mantle-normalized trace element variation diagram, most gabbro samples are enriched in large-ion lithophile elements (LILEs; e.g., Sr, Ba, and U) and slightly depleted in high field strength elements (HFSEs; e.g., Nb, Ta, Zr and Hf) (Fig. 5b).

The basalt samples from the Adaatsag ophiolite have SiO_2 contents of 45.99–52.06 wt%, and Al_2O_3, MgO, Na_2O, K_2O, and TiO_2 contents of 14.24–17.24 wt%, 4.95–7.88 wt%, 1.43–3.54 wt%, 0.05–0.07 wt%, and 1.17–2.00 wt%, respectively. The $Mg^{\#}$ values range from 0.46 and 0.61.

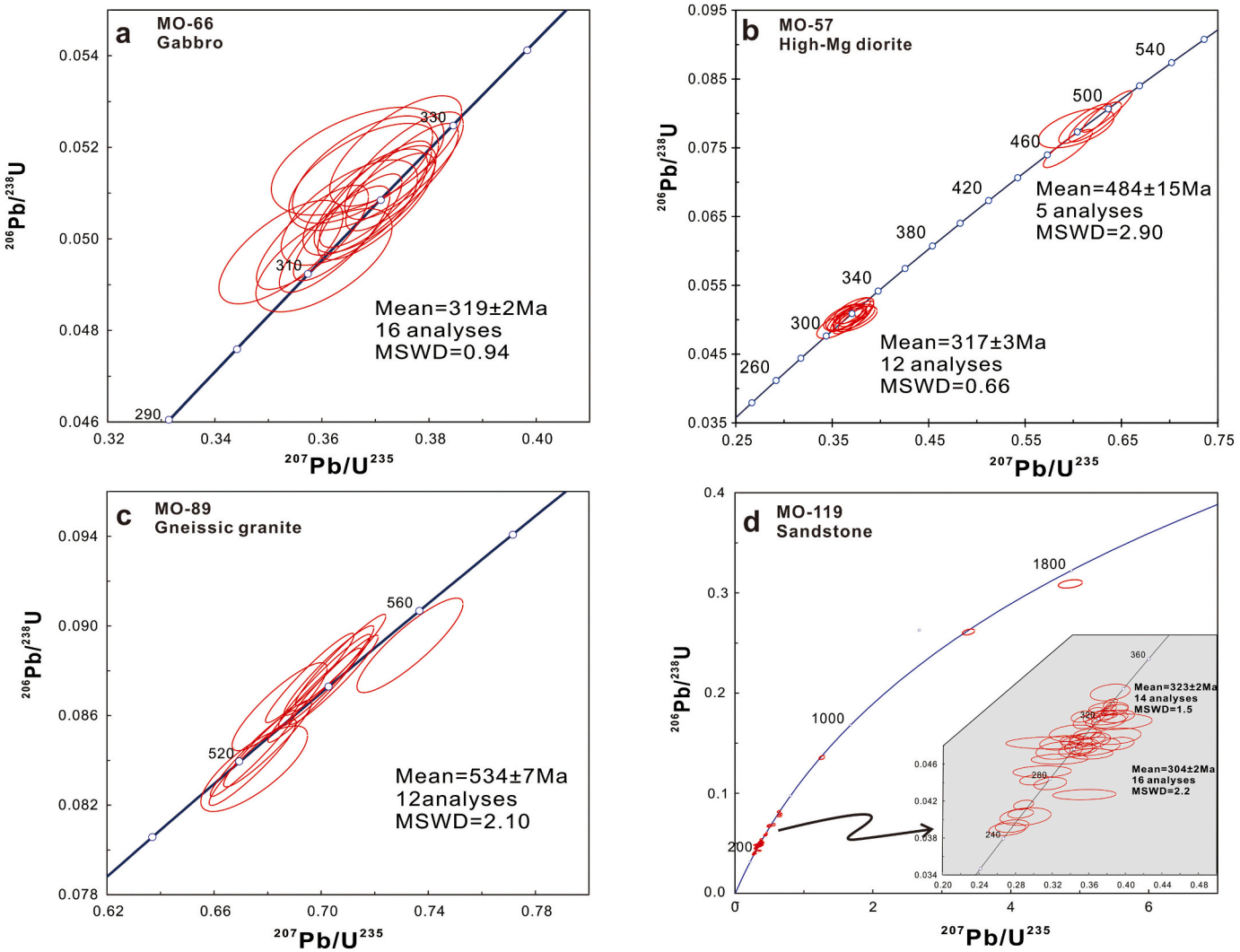

Fig. 7. Zircon U—Pb concordia diagrams for (a) Gabbro (MO-66) of the Adaatsag ophiolite, (b) High-Mg diorite (MO-57), (c) Gneissic granite (MO-89) underlying the Adaatsag ophiolite, and (d) Sandstone from the late Permian Horinj Formation (MO-119).

In the Zr/TiO_2 vs. Nb/Y and FeO^T – Na_2O + K_2O–MgO diagrams, all basalt samples plot in the tholeiitic basalt field, close to the FAB samples of IBM forearc (Fig. 4a, b). They have REE contents ranging from 34 to 59 ppm, with distinct LREE depletion [$(La/Yb)_N$ of 0.39–0.80] and negligible Eu anomalies (Eu/Eu* =0.89–1.11) (Fig. 5c). In a primitive mantle normalized trace-element variation diagram, the samples are slightly enriched in LILEs (e.g., U and Ba) and show minor negative anomalies in Nb and Ta, overlapping with the IBM FAB samples (Fig. 5d).

The quartz diorite samples have high MgO (4.35–6.66 wt%), $Mg^{\#}$ (0.57–0.69), $Fe_2O_3^T$ (4.67–7.81 wt%), moderate SiO_2 (54.98–64.78 wt %), and low TiO_2 (0.31–0.40 wt%) concentrations. They are also rich in Cr (131–279 ppm) and Ni (55–94 ppm). In the SiO_2–$Mg^{\#}$ and SiO_2–MgO diagrams (Fig. 4c, d), all the samples plot in the HMA area, close to the HMA samples of the IBM arc. The samples show REE contents of 19–25 ppm, and the chondrite-normalized REE patterns of the samples are slightly fractionated and display a negative slope with depletion of HREE [$(La/Yb)_N$ = 1.41–4.20)] and no Eu anomalies (Eu/Eu* = 0.96–1.08) (Fig. 5e). They exhibit negative Nb, Ta and Ti anomalies in primitive - mantle - normalized trace element diagrams identical to the HMA samples of the IBM arc, but with higher Ba, Th and Sr contents (Fig. 5f).

5.2. Zircon U—Pb geochronology

One gabbro sample, one high-Mg diorite and one gneissic granitic sample were selected for SIMS U—Pb zircon dating. One sample from the Permian sandstone was chosen for LA-ICPMS U—Pb detrital zircon dating. The analytical results are presented in Table S2 and Table S3.

Zircons from the gabbro sample MO-66 collected from the Adaatsag ophiolite are euhedral to subhedral prisms that are 100–200 μm long. Most zircons show oscillatory zoning (Fig. 6a), which is characteristic of igneous zircon (e.g., Rubatto, 2002). Seventeen zircon grains were chosen for analysis. The measured U and Th concentrations vary from 92 to 415 ppm and from 25 to 393 ppm, respectively, with Th/U ratios between 0.17 and 1.23, typically indicating igneous origin (e.g., Rubatto, 2002). Sixteen analyses yielded a weighted mean $^{206}Pb/^{238}U$ age of 319 ± 2 Ma (MSWD = 0.94; Fig. 7a), which is interpreted as the crystallization time of zircons. One spot analysis yielded an older age of ca. 499 Ma, which is interpreted to represent zircon inheritance.

Zircons from the high-Mg diorite sample MO-57 intruding the gabbro of the Adaatsag ophiolite are 80–150 μm in size with length/width ratios of 1:1 to 2:1. Most zircons show typical oscillatory zoning (Fig. 6b). The measured U and Th concentrations vary from 39 to 1359 ppm and from 11 to 1099 ppm, respectively. Their Th/U ratios range from 0.27 to 1.27, indicating a magmatic origin for the zircons. Seventeen zircon grains were dated, and twelve analyses yielded a concordia weighted mean

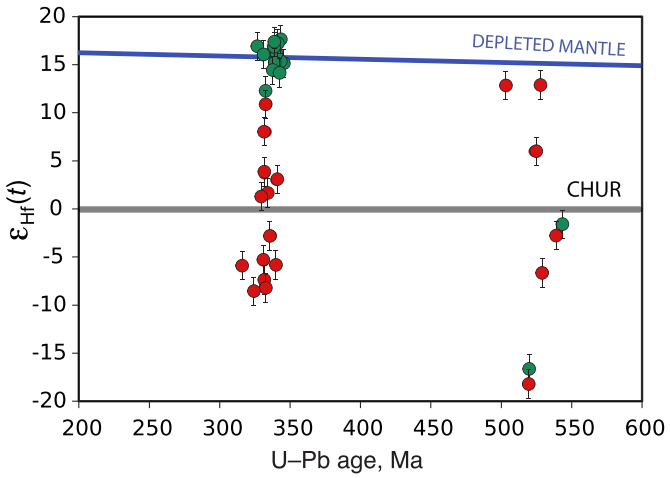

Fig. 8. Zircon U—Pb age vs. $\varepsilon_{Hf(t)}$ diagram for the gabbro and high-Mg diorite of the Adaatsag ophiolite.

$^{206}Pb/^{238}U$ age of 317 ± 3 Ma (MSWD = 0.66; Fig. 7b), which is interpreted to record the time of igneous crystallization of the high-Mg diorite. Five spot analysis yielded a concordia weighted mean $^{206}Pb/^{238}U$ age of 484 ± 15 Ma (MSWD = 2.90; Fig. 7b), which we interpret as an inherited zircon.

Zircons from the gneissic granite sample MO-89 collected from the North Gobi Formation structurally underlying the Adaatsag ophiolite are 80–150 μm in size with length/width ratios of 1:1 to 2:1. Most zircons show typical oscillatory zoning (Fig. 6c). The measured U and Th concentrations vary from 187 to 2025 ppm and from 45 to 546 ppm, respectively. Their Th/U ratios range from 0.06 to 0.82, indicating a magmatic origin for the zircons. Thirteen zircon grains were chosen for age analyses, and twelve spot analysis yielded a concordia weighted mean $^{206}Pb/^{238}U$ age of 534 ± 7 Ma (MSWD = 2.10; Fig. 7c), which is interpreted to record the time of igneous crystallization of the gneissic granite. One spot analysis yields an older age of ca. 870 Ma, which is interpreted to represent zircon inheritance.

Zircons from the sandstone sample MO-119 collected from the Late Permian Horinj Formation are rounded to subhedral and range from 100 to 200 μm in size. CL imaging reveals that most grains have oscillatory or planar-banded growth zones (Fig. 6d), indicating a magmatic origin. A total of 53 U-Pb analyses were obtained, and they have U and Th contents and Th/U ratios ranging from 54 to 2710 ppm, 31 to 906 ppm and 0.04 to 1.20, respectively. All the analysis yielded ages ranging from 246 ± 3 Ma to 1865 ± 42 Ma, which cluster in three main age groups: (1) U—Pb ages of 246–257 with a minor peak at 252 Ma, (2) 297–311 Ma with a peak at 304 Ma, (3) 318–328 Ma with a peak at 323 Ma (Fig. 7d).

5.3. Zircon Hf analyses

Zircon Hf analyses were performed for the gabbro and high-Mg diorite samples on the same spots as U—Pb age data, and the results are listed in Table S4 and shown in Fig. 8. Sixteen zircon grains were analyzed for the gabbro sample. The zircons with young ages (312–326 Ma) have high initial $^{176}Hf/^{177}Hf$ ratios, positive $\varepsilon_{Hf}(t)$ values (+12.2 – +17.7), and young model ages T_{DM} (249–460 Ma). The inherited zircon (ca. 499 Ma) has a negative $\varepsilon_{Hf}(t)$ value (−1.6), and a far older model age T_{DM} (ca. 1162 Ma). Eighteen zircon grains were analyzed for the high-Mg diorite sample. The zircons with younger ages (301–323 Ma) yield highly variable $^{176}Hf/^{177}Hf$ ratios and $\varepsilon_{Hf}(t)$ values(−8.5 – +11.0), and variable model ages T_{DM} (514–1281 Ma). The inherited zircons (466–498 Ma) display variable $\varepsilon_{Hf}(t)$ values(−6.6 – +12.9) and model ages T_{DM} (563–1343 Ma).

6. Discussion

6.1. Formation/emplacement ages of the Adaatsag ophiolite

The layered gabbro from the Adaatsag ophiolite yielded a SIMS zircon U—Pb age of 319 ± 2 Ma. Since the analyzed zircons show a magmatic origin, we interpret the U—Pb age as the crystallization time. This age is comparable with the single-zircon evaporation age of ca. 325 Ma from the leucogabbro pegmatite dyke in the same ophiolite (Tomurtogoo et al., 2005). The recently discovered Khuhu Davaa ophiolitic body along the Adaatsag suture zone (Zhu et al., 2018) could represent the northeastward extension of the Adaatsag. Both ophiolitic bodies formed concomitantly: Metagabbro and plagiogranite samples from the Khuhu Davaa ophiolite yielded SIMS zircon U—Pb ages of 321 ± 4 Ma and 314 ± 3 Ma. The older zircon grains (499–870 Ma; Zhu et al., 2018) from both ophiolites possibly derived from sheared crustal material or delaminated continental lithosphere during the opening of the MOO, or from the continental crust trapped within fracture zones by a series of transform migrations and ridge jumps (Pilot et al., 1998).

Zircons from the gneissic granite structurally underlying the Adaatsag ophiolite yielded ca. 534 Ma. This indicates that the ophiolite probably emplaced onto the Early–Middle Paleozoic tectonic domain of the Ereendavaa terrane as an allochthonous unit. The Kherlen ophiolitic complex has been interpreted to mark a suture zone between the Ereendavaa terrane and the Idermeg terrane (Miao et al., 2017; Narantsetseg et al., 2019). The northward subduction of the Kherlen Ocean is documented by the numerous subduction-related magmatic records developed in the Ereendavaa terrane at least from the Late Cambrian to the Late Ordovician (ca. 512–455 Ma) (Narantsetseg et al., 2019; Orolmaa et al., 2015). This gneissic granite likely belongs to this Early Paleozoic magmatic arc.

The Late Permian molassic sequences of the Horinj Formation unconformably overlie the tectonic contacts between the allochthonous Adaatsag ophiolites and the Ereendavaa terrane. The conglomerates contain clasts of plagiogranite and red chert possibly derived from the ophiolite they unconformably overlie. These facts indicate that the molassic sequences postdate but are closely related to the ophiolite emplacement. The youngest zircon peak found in the molassic sequences is 252 Ma, which suggest a Permo-Triassic time for its deposition. Since the molasses contain fragments of the ophiolite, its emplacement is restricted to sometime before 252 Ma. The detrital age group of 318–328 Ma (peak at 323 Ma) found in the Horinj Formation is interpreted to be derived from the Adaatsag ophiolite, and the age group of 297–311 Ma with a peak at 304 Ma probably represents the later superimposed subduction-related magmatic rocks. The age spectra of 418–427 Ma is likely sourced from the Early Devonian (ca. 418–409 Ma) bimodal volcanic suite in the Ereendavaa terrane, which was interpreted to be formed by the post-collisional break-off of the subducted Kherlen Ocean slab (Narantsetseg et al., 2019). The detrital zircons with ages of 481–1865 Ma probably originated from the Precambrian crystalline basement and the Early–Middle Paleozoic subduction-related magmatic rocks of the Ereendavaa terrane. Our results suggest that the unconformably overlying Permo-Triassic molassic sediments are sourced from both the Ereendavaa terrane and the Adaatsag ophiolite, implying that the ophiolite accreted to the Ereendavaa terrane during this period.

6.2. Petrogenesis and tectonic setting

The petrographic observations and geochemical data suggest that the samples in this study experienced various degree of hydrothermal alteration. We found no linear correlation between the Loss on Ignition (LOI) and several major element oxides (SiO_2, MgO, TiO_2 (not shown) and Na_2O, Fig. 9a–c). This indicates that they were generally immobile during alteration (Nakamura et al., 2007). Zirconium is considered as one of the least mobile elements and thus used as a reference to monitor the mobility of the other trace elements (Pearce, 2014). The elements

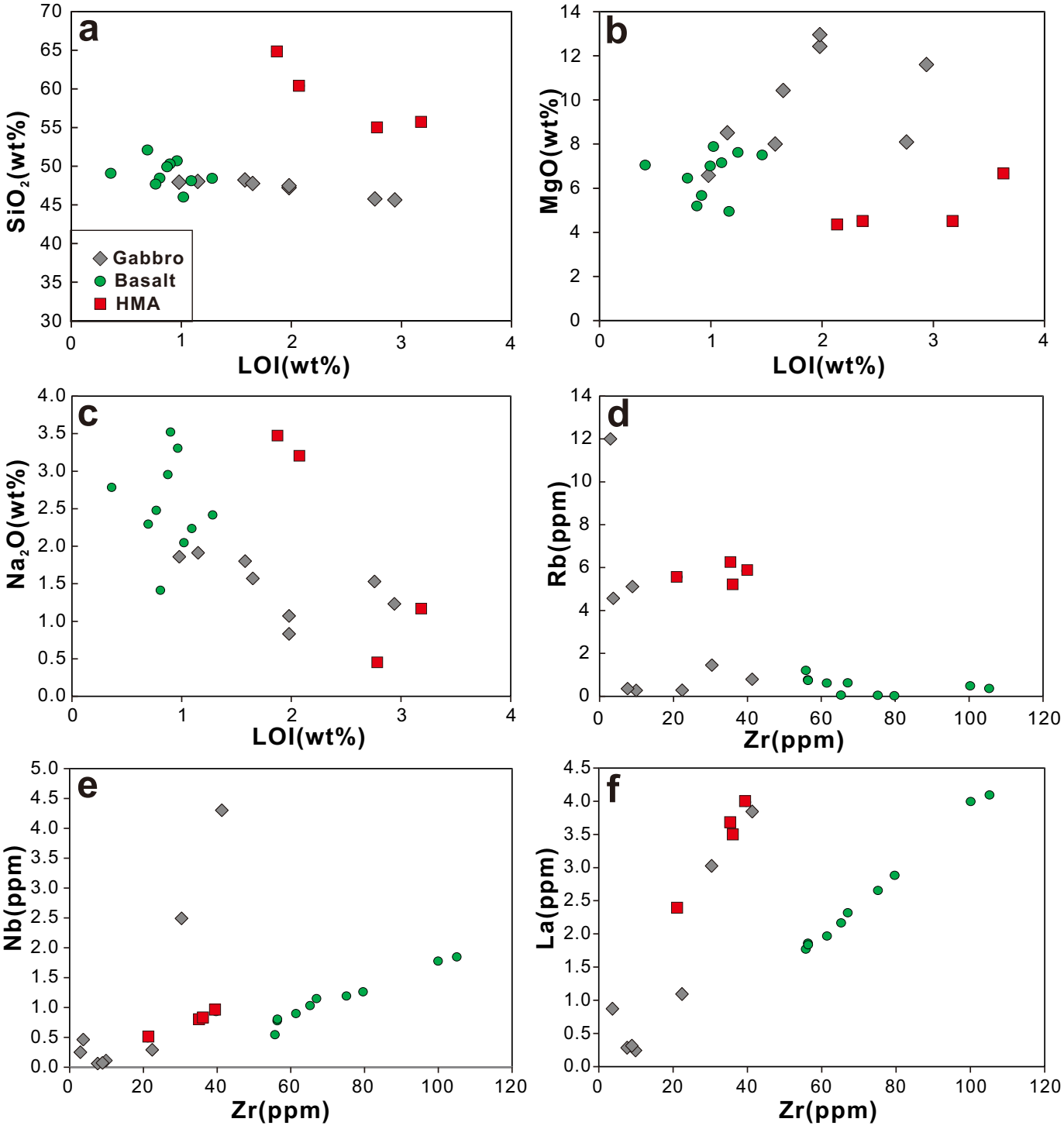

Fig. 9. Plots of selected elements versus LOI or Zr to evaluate the mobility of these elements.

Nb, La, and Th have well-defined linear relationships relative to Zr, while some elements such as Rb and Pb (not shown), show large scatter (Fig. 9d–f). Considering the relatively low LOI (most of them <2 wt%), we suggest that the samples in this study generally preserved their original geochemical characteristics.

The studied harzburgites from the Adaatsag ophiolite have refractory compositions, i.e., low contents of CaO, Al_2O_3, Na_2O and TiO_2, but relatively high MgO contents. According to the melting trends calculated from a depleted mantle source (Niu, 1997), the Adaatsag harzburgites are estimated to have been subjected to 15–20% of partial melting (Fig. 10). Mantle-derived magmas are often contaminated by continental crust during magma ascent. However, we found no correlation of Nb/La and Th/La with SiO_2, and the very low Th/Ce (0.01–0.02) and Th/La (0.04–0.06) ratios, which rules out significant crustal contamination of the basalts (Fig. 11a, b). Similarly, the Th/Ta ratios of the basalts range from 1.00 to 1.65, which are relatively close to the primitive mantle value (Th/Ta = 2.3), but very different from the continental crust value (Th/Ta = 10) (Sun and McDonough, 1989), implying negligible crustal contamination. The basalt samples have lower Mg# (0.46–0.61), Cr (9–291 ppm) and Ni (15–78 ppm) than those in a

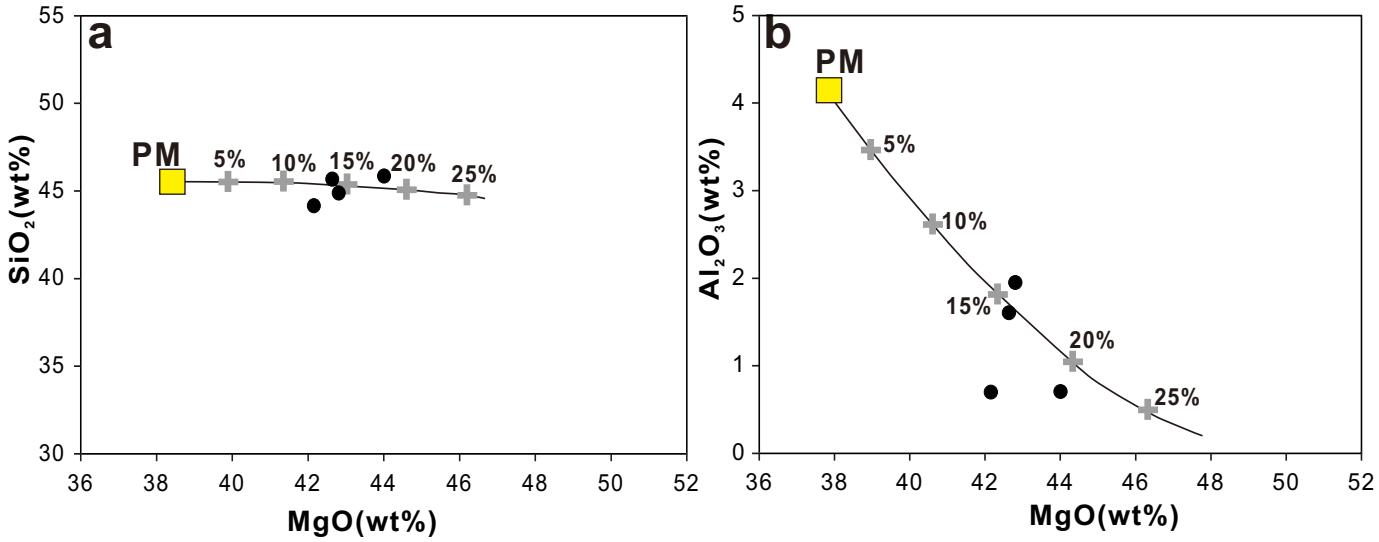

Fig. 10. Whole rock major elements of the harzburgites of the Adaatsag ophiolite. The polybaric near-fractional (1% melt porosity) melting curves are presented using the model of Niu (1997). PM: primitive mantle.

primitive mantle-derived magma, indicating an evolved composition. The basalt shows a positive correlation of Cr and Ni contents against values of Mg#, suggesting the fractional crystallization of olivine and clinopyroxene in the mafic magma (Fig. 11c, d). Because of the differences in partition coefficients, the Ni vs. Cr and V vs. Cr diagrams can be used to distinguish between the fractional crystallization of olivine, clinopyroxene, and hornblende (Rollinson, 1993). It appears that fractional crystallization of clinopyroxene rather than olivine or hornblende played a major role during their magmatic evolution (Fig. 11e, f). The lack of correlation between the Dy/Yb ratios and SiO_2 contents further indicates that amphibole fractionation did not play a major role (Fig. 11g; Davidson et al., 2007). We found no Eu anomalies ($Eu/Eu^* = 0.89–1.11$), denoting a weak fractional crystallization or accumulation of plagioclase. The lack of correlation between TiO_2 and MgO indicates that Fe—Ti oxide fractionation was insignificant (Fig. 11h).

The gabbro and tholeiitic basalts from the Adaatsag ophiolite show depleted mid-ocean ridge basalts (N-MORB) geochemical features, indicating that they originated from a depleted mantle reservoir (e.g., Sun and McDonough, 1989). This conclusion is further supported by a series of tectono-magmatic discrimination diagrams (Fig. 12a, b, c). However, when compared with MORB, our basaltic samples show lower HFSE contents (Nb and Ta), which are comparable to the FABs (Fig. 5 a–d) (Hickey-Vargas et al., 2018; Li et al., 2020; Reagan et al., 2010). They also exhibit slight enrichment in LILEs (Ba and U), indicating some input of slab-derived material (Stern, 2002). This inference is reinforced by plots in the Nb/Yb vs. Th/Yb diagram, where some basalt samples lie slightly above the mantle array (Fig. 12a). In the Nb_N vs. Th_N diagram (Saccani, 2015), most samples straddle the boundary between the N-MORB field and fore-arc fields (Fig. 12c). In addtion, the gabbro samples exhibit HFS*E*-depletion and LILE-enrichment, which are typical features of arc magmatism. We interpret that the Adaatsag ophiolite formed in an intra-oceanic forearc tectonic setting.

The Adaatsag high-Mg diorites have geochemical affinities to the typical HMAs, probably representing the intrusive equivalents of the HMAs. The HMAs are generally divided into four subtypes: high-Mg adakite, bajaite, boninite and sanukitoid (e.g., Kamei et al., 2004; Smithies and Champion, 2000). The Adaatsag high-Mg diorites have relatively low Sr (223–368 ppm) contents, Sr/Y (24–32) and $(La/Yb)_N$ (1.41–4.20), which distinguish them from high-Mg adakites and Bajaites (Fig. 12d). They yield relatively lower MgO (4.35–6.66 wt%) compared with the typical boninite (MgO > 8 wt%), relatively lower TiO_2 and Y contents than the sanukitoid (TiO_2 > 0.38 wt% and Y > 9 ppm) (Kamei et al., 2004; Macpherson and Hall, 2001), showing a transitional affinity between sanukites and boninite, close to the HMA samples of the IBM arc (Fig. 12d). There are generally four genetic models for HMAs: (1) partial melting of the mantle peridotite material (Straub et al., 2011); (2) interaction of mantle materials and delaminated lower continental crust (Gao et al., 2004); (3) the mixing of felsic and mafic or ultramafic magmas (Qian and Hermann, 2010), and (4) partial melting of the mantle wedge modified by interaction with the subducting slab (e.g., Tatsumi, 2001; Zeng et al., 2016).

We can rule out the model (1) (direct melting of the depleted mantle), because the Adaatsag high-Mg diorite has high SiO_2 content relative to typical mantle peridotite sources (SiO_2 < 55%; Mitchell and Grove, 2015), and shows various negative zircon $\varepsilon_{Hf}(t)$ rather than the depleted isotopic signatures. Model (2) (the interaction of mantle materials and delaminated lower continental crust) can be precluded, because partial melting of lower continental crust generally produces adakitic magmas with high Sr and low Y and Yb contents (e.g., Qian and Hermann, 2010), which are at odds with the Adaatsag high-Mg diorite (Fig. 12d). Model (3) (magma mixing) generally produces linear variations in most major and trace elements with increasing SiO_2 in binary plots, but the Adaatsag diorite do not exhibit this feature (Fig. S1). The absence of mantle enclaves indicates the Adaatsag diorite likely did not form by mantle and crust derived melt assimilation (e.g., Qian and Hermann, 2010). We have found no incompatibilities with our dataset and the fourth model. Therefore, combined with their arc-type geochemical characteristics, we suggest the Adaatsag diorites originated form partial melting of the mantle wedge modified by interaction with subducting slab.

The Carboniferous SSZ-type Adaatsag ophiolites and coeval high-Mg diorite provide evidence for the existence of an intra-oceanic subduction-accretion system in the Southwest MOO during the Carboniferous. The older inherited zircon age and variable negative $\varepsilon_{Hf}(t)$ data indicate that a continental sliver or fragment probably existed below the intra-oceanic arc.

6.3. *Tectonic evolution of the MOO*

Our new results have important implications for the subduction initiation of the MOO. The Adaatsag basalts only show slight enrichment in LILEs compared to HREEs and HFSEs, and have slightly lower Nb and Ta contents than that of N-MORB, indicating limited input from slab-derived material. The Khuhu Davaa ophiolite, interpreted as the

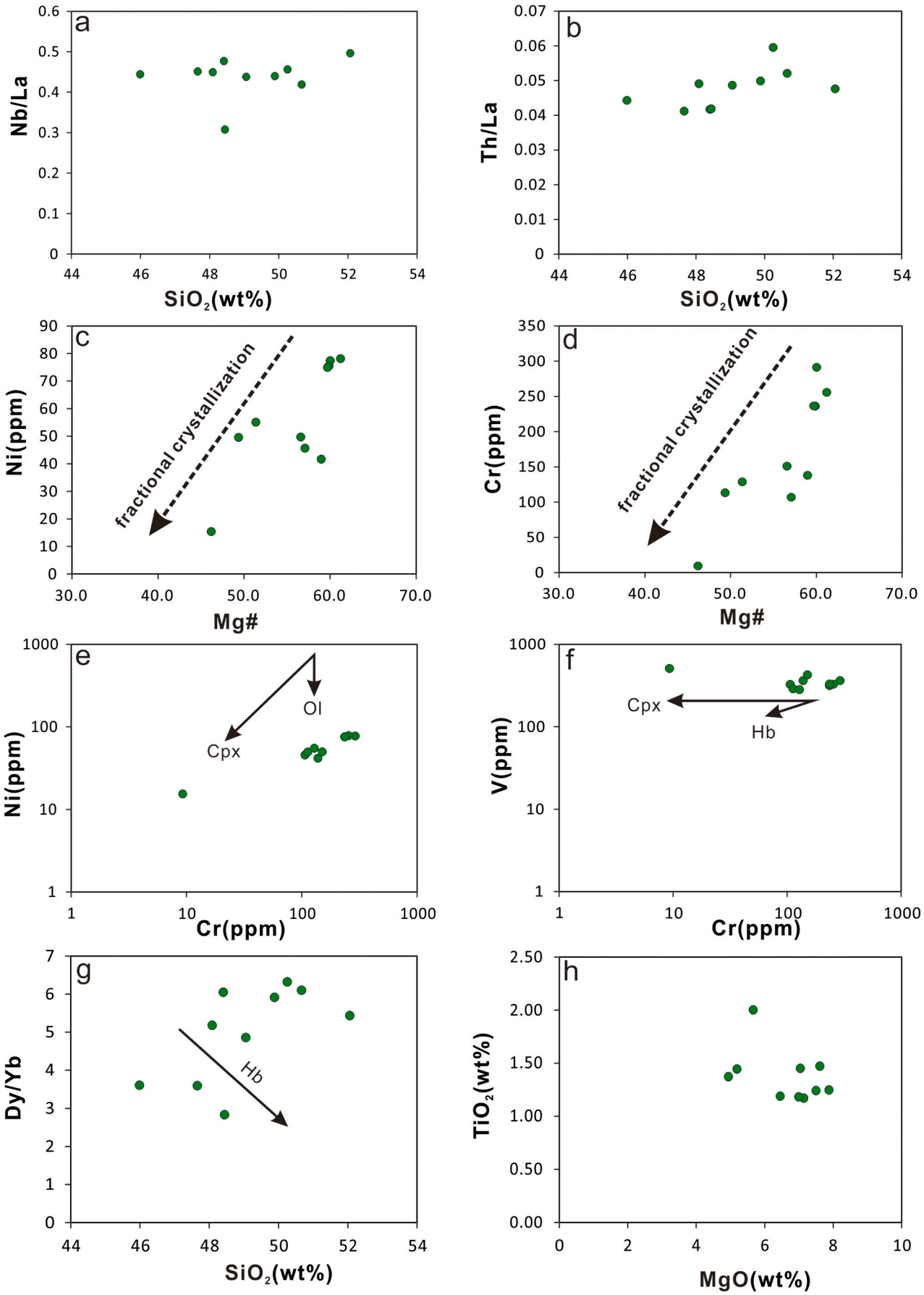

Fig. 11. Selected elements and their ratios plots for the basalts of the Adaatsag ophiolite.

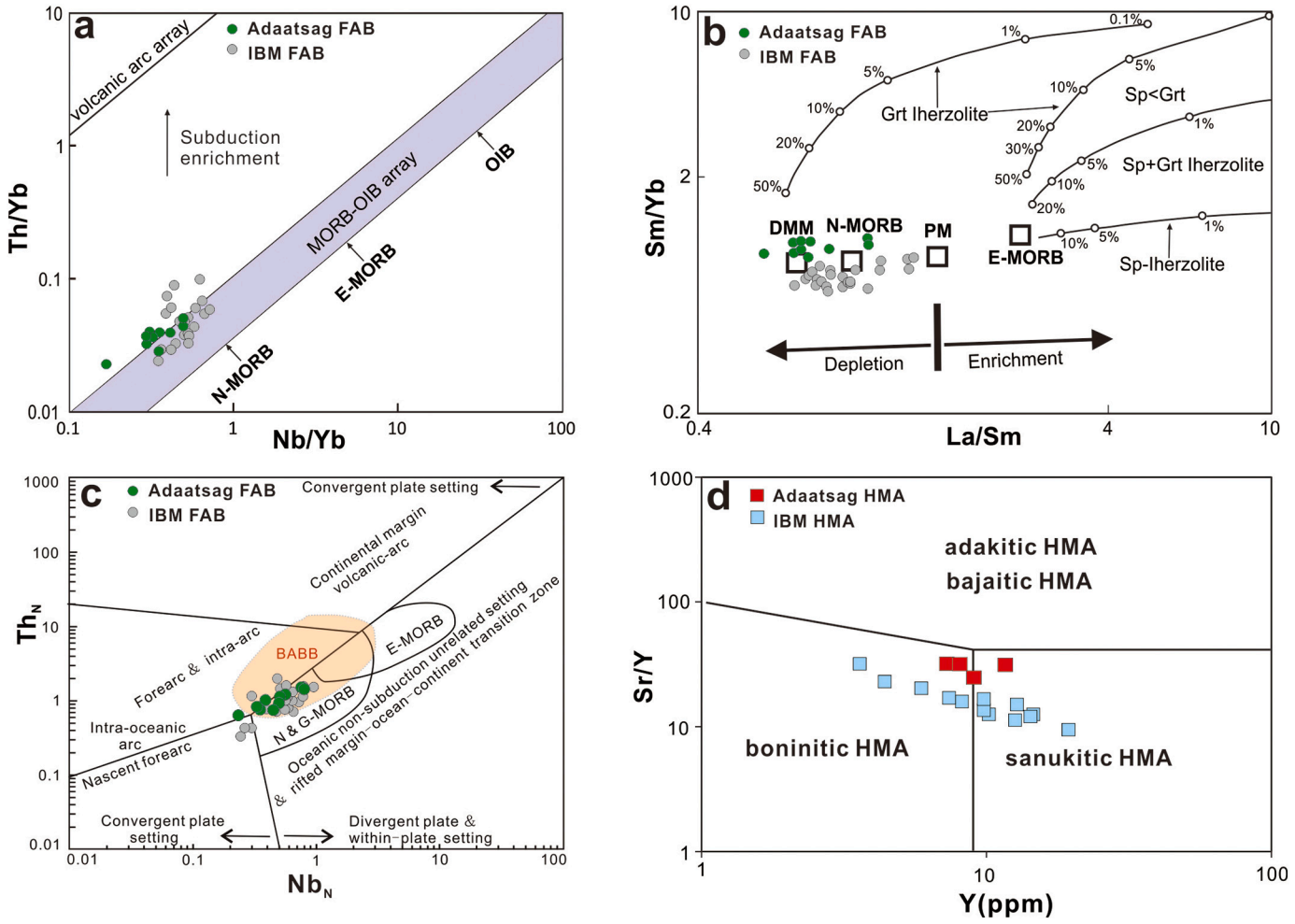

Fig. 12. Geochemical plots of the basalt and high-Mg diorite from the Adaatsag ophiolite. (a) Th/Yb vs. Nb/Yb for the basalt (Pearce, 2008). (b) Sm/Yb vs. La/Sm for the basalt (Aldanmaz et al., 2000). (c) Nb_N vs Th_N for the basalt (Saccani, 2015). (d) Sr/Y vs. Y discrimination diagram for the high-Mg diorite (Kamei et al., 2004). Data sources of IBM forearc basalts and high-Mg andesites are from Reagan et al. (2010) and Shervais et al. (2021), respectively. Normalizing values are from Sun and McDonough (1989).

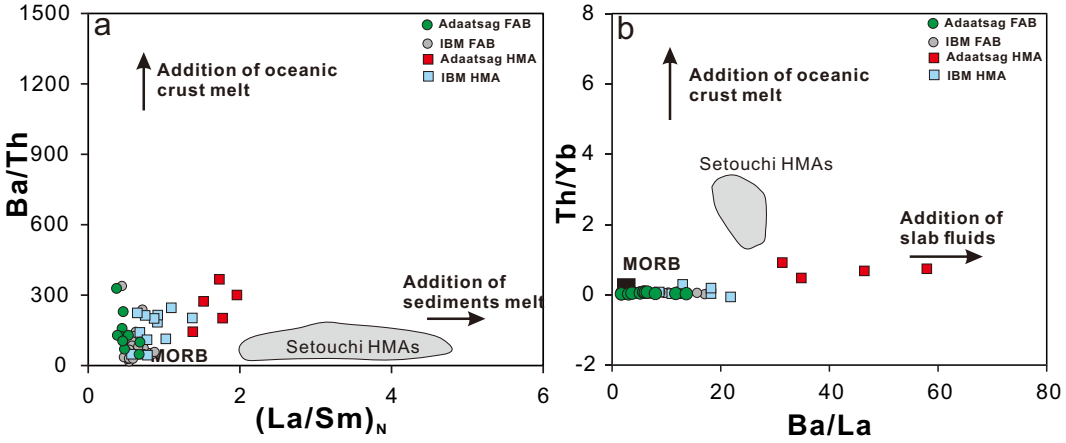

Fig. 13. (a) Plots of Ba/Th vs $(La/Sm)_N$ (after Labanieh et al., 2012) and (b) Plots of Th/Yb vs Ba/La (after Woodhead et al., 2001) of the basalt and high-Mg diorite of the Adaatsag ophiolite. Data sources of IBM forearc basalts and high-Mg andesites are from Reagan et al. (2010) and Shervais et al. (2021), respectively.

northeast counterpart of the Adaatsag ophiolite within the suture zone, show very similar features. Tholeiitic basalt samples from the Khuhu Davaa ophiolite show N-MORB and E-MORB geochemical affinities, but are enriched in Ba, Pb and Sr, and no Nb and Ta depletion, which reflect a limited mass transfer from the subducting plate (Zhu et al., 2018). All these data suggest that the basaltic rocks from the ophiolites are geochemically akin to the FABs, which are considered the first lavas to erupt after subduction initiation (Ishizuka et al., 2014; Reagan et al.,

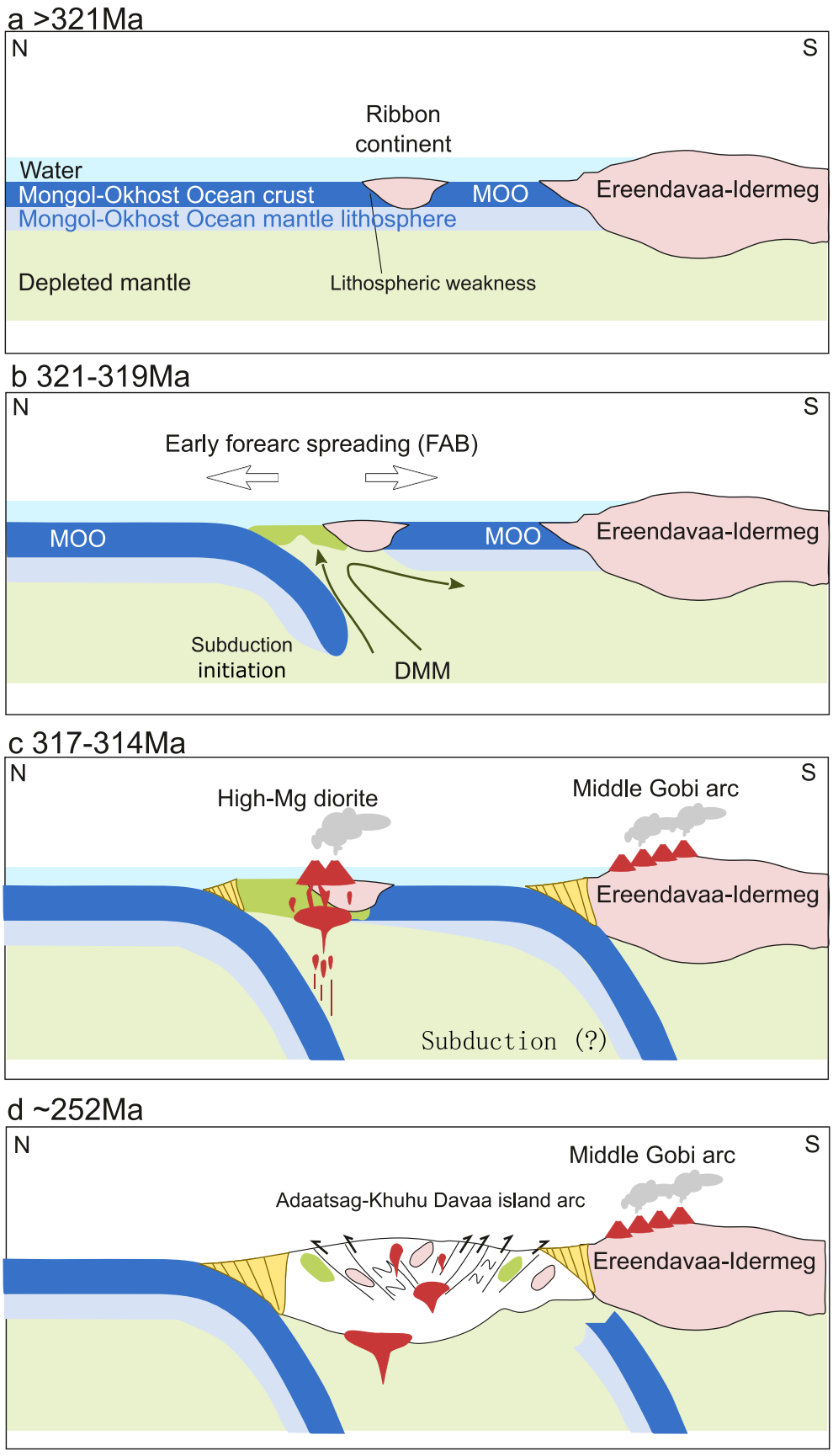

Fig. 14. Schematic diagrams showing the proposed tectonic evolution of the Mongol–Okhotsk Ocean, from subduction initiation to arc-continent collision.

2010).

In contrast, the Adaatsag high-Mg diorites display enrichment of LILEs and LREEs and distinct depletion of HFSEs, indicating increased metasomatism from slab-derived materials, similar to the HMAs from the IBM arc. It has been suggested that a mantle wedge can be modified by enriched components, such as LILEs-rich fluids, subducted sediment melts and altered oceanic crust melts, under an arc magma system (e.g., Hanyu et al., 2002; Karsli et al., 2017; Tatsumi, 2006). Elements such as La, Yb, and Th that partition differently in subduction-zone-derived fluids and melts can be used to monitor the involvement of different materials during magma genesis (Woodhead et al., 2001). Addition of sediment-derived melts could notably enhance the La/Sm ratios of the magma, but cannot change the Ba/Th ratios (Tatsumi, 2006), which are consistent with the features of the Adaatsag high-Mg diorites (Fig. 13a). The Ba/La ratios would also be elevated accordingly if additional fluids were involved, because Ba is more soluble in aqueous fluids than La (Hanyu et al., 2006). As presented in Fig. 13b, we infer that H_2O-rich fluids are probably another metasomatic agent involved in the production of the Adaatsag high-Mg dioritic magmas. These data reflect a progressive transition from the FABs to high-Mg diorite with a transitional geochemical affinity between sanukites and boninite, akin to the evolution of the IBM forearc (Hickey-Vargas et al., 2018; Ishizuka et al., 2014; Reagan et al., 2010).

Decompression melting of a depleted MORB-type mantle was followed by melting of a mantle source that was metasomatized by slab-derived fluid and sediment-derived melts. These magmatic records preserved in the Adaatsag ophiolite suggest a progression from less to more HFSE-depleted and from less to more slab-metasomatized with time, thus adhering to the "subduction initial rule" (e.g., Whattam and Stern, 2011). In the IBM intra-oceanic arc system, the change from subduction initiation to flux melting (boninitic volcanism) takes 2–4 Ma, and the subsequent change to flux melting in the counterflowing mantle (normal arc magmatism) takes 7–8 Ma (Gurnis et al., 2004; Ishizuka et al., 2011). In the Adaatsag opholite, the change from the FABs (ca. 319 Ma) to the high-Mg diorite (ca. 317 Ma) took about 2 Ma. In the Khuhu Davaa ophiolite, the change from the FABs (ca. 321 Ma) to the plagiogranite (ca. 314 Ma) formed by the partial melting of the mafic oceanic crust took about 7 Ma. The magmatic progression and their timescales in the Adaatsag and Khuhu Davaa ophiolite mimic that of the subduction initiation of the Mariana forearc. Therefore, we interpret that the Adaatsag SSZ ophiolites are the relic of an Early Pennsylvanian subduction initiation process that occurred within the Southwest MOO. The occurrences of these two ophiolites suggest that the Carboniferous subduction initiation zone extended at least 200 km.

The presence of older zircons with negative $\varepsilon_{Hf}(t)$ isotope data in both ophiolitic bodies implies the inheritance of zircons from a piece of continental crust. It is tempting to speculate that the passive continental margins collapse to form the new subduction zones to explain these features. However, numerical modeling and natural observations have shown that it is difficult to initiate subduction at passive continental margins due to the high rheological strength that resists the lithospheric collapse, like the stable Atlantic passive margin (e.g., Gurnis et al., 2004). Moreover, as mentioned above, the geochemical data indicate that the two SSZ ophiolites generally formed in an intra-oceanic tectonic setting. We suggest that the Adaatsag– Khuhu Davaa intra-oceanic arc was likely underlain in part by a continental sliver or relic. The inherited zircons (484–870 Ma) show U—Pb ages comparable to those of zircons recovered from the Ereendavaa terrane (Miao et al., 2017; Narantsetseg et al., 2019). We propose that a thin continent sliver was rifted apart from the Idermeg–Ereendavaa unified composite terrane during the opening of the MOO. Some modern arcs contain old trapped zircon xenocrysts in juvenile oceanic rocks such as the Solomon Islands (Tapster et al., 2014) and the Luzon arc (Shao et al., 2015). This feature has been identified as well in ancient oceanic arcs (Li et al., 2018). Some previous studies emphasize the importance of transform faults and fracture zones for the nucleation of subduction initiation in intra-oceanic subduction systems (e.g., Stern and Gerya, 2018). In this study, we consider that the presence of a sliver of continental crust could trigger, or at least facilitated, the initiation of southward subduction of the MOO plate, similar to the case in the Luzon intra-oceanic arc system (Shao et al., 2015).

Based on our results and the published literature, we propose a tectonic evolution model for the southern margin of the MOO in the Mongolia segment (Fig. 14). During the opening of the MOO, thin and elongated fragments of continents (ribbons) splited off the Idermeg–Ereendavaa margin (Fig. 14a). This ribbon continent-ocean boundary might have represented a lithospheric weakness or a heterogeneity easier to exploit during the kinematic changes that trigger the initiation of new subduction zones. During the Early Pennsylvanian, the sinking lithosphere slab may have caused rapid trench rollback, allowing the asthenosphere to flood over the sinking slab (Fig. 14b). Asthenospheric upwelling and subsequent decompression melting (Stern and Gerya, 2018) produced MORB-like FABs (321–319 Ma) in the Adaatsag and Khuhu Davaa ophiolites. These FAB magmas picked up older zircons from the continental ribbon during the magma rise and/or in the magma chamber. After some time (2–7 Ma), fluids and melts from the sinking slab caused the overlying mantle wedge (including the depleted mantle and the continental lithospheric mantle) melt to generate high-Mg diorite (~317 Ma) (Fig. 14c). The northern margin of the Idermeg–Ereendavaa terrane possibly turned into an active continental margin during the Carboniferous (Badarch et al., 2002; Bussien et al., 2011; Sun et al., 2013; Zhu et al., 2022). As subduction continued, the Adaatsag and Khuhu Davaa ophiolites were emplaced onto the northern edge of the Idermeg–Ereendavaa terrane due to the arc-continent collision (>252 Ma) (Fig. 14d). The Permo-Triassic molassic sequences are considered to reflect this ophiolite southward emplacement.

7. Conclusions

The forearc basalts and high-Mg diorite in the Adaatsag ophiolite record a subduction progression from less to more slab-metasomatism within a short time window, analogous to the evolution of the Izu-Bonin-Mariana forearc. Combined with the northeastern counterpart of the Khuhu Davaa ophiolite, these findings could mark the initial subduction of the Mongol–Okhotsk Ocean in its southwestern part during the Early Pennsylvanian (ca. 321–319 Ma). The underlying gneissic granite and the overlying molassic sequences in Adaatsag indicate that the Adaatsag ophiolite was emplaced as allochthones onto the Early–Middle Paleozoic basement of the Ereendavaa terrane before ca. 252 Ma. The presence of a continent fragment evidenced by the xenocrystal zircons and negative zircon Hf isotope data of the ophiolite likely facilitated the initiation of subduction.

Declaration of Competing Interest

The authors declare that they have no known competing financial interests or personal relationships that could have appeared to influence the work reported in this paper.

Acknowledgments

We are grateful to Chun Yang, Mingzhu Ma, Liqin Zhou, Xiaochao Che, Chenghao Liu and Shuangrong Zhang for their supports of the analytical experiments. We thank Munkhtsengel Baatar and Chimedtseren Anaad for their supports during our field investigations in Mongolia. This work was financially supported by Strategic Priority Research Program of Chinese Academy of Sciences (grant No. XDB 41000000), the National Natural Science Foundation of China (grant No. 42272262), the Second Tibetan Plateau Scientific Expedition and Research Program (Grant No. 2019QZKK0806) and Ramón y Cajal Fellowship from the Spanish Ministry of Science and Innovation.

Appendix A. Supplementary data

Supplementary data to this article can be found online at https://doi.org/10.1016/j.lithos.2022.106951.

References

Aldanmaz, E., Pearce, J.A., Thirwall, M.F., Mitchell, J.G., 2000. Petrogenetic evolution of late Cenozoic post-collision volcanism in western Anatolia, Turkey. J. Volcanol. Geotherm. Res. 102, 67–95.

Arculus, R.J., Ishizuka, O., Bogus, K.A., Gurnis, M., Hickey-Vargas, R., Aljahdali, M.H., Bandini-Maeder, A.N., Barth, A.P., Brandl, P.A., Drab, L., do Monte Guerra, R., Hamada, M., Jiang, F., Kanayama, K., Kender, S., Kusano, Y., Li, H., Loudin, L.C., Maffione, M., Marsaglia, K.M., McCarthy, A., Meffre, S., Morris, A., Neuhaus, M., Savov, I.P., Sena, C., Tepley III, F.J., van der Land, C., Yogodzinski, G.M., Zhang, Z., 2015. A record of spontaneous subduction initiation in the Izu–Bonin–Mariana Arc. Nat. Geosci. 8, 728–733.

Badarch, G., Cunningham, W.D., Windley, B.F., 2002. A new terrane subdivision for Mongolia: Implications for the Phanerozoic crustal growth of Central Asia. J. Asian Earth Sci. 21, 87–104.

Bussien, D., Gombojav, N., Winkler, W., Quadt, A., 2011. The Mongol–Okhotsk Belt in Mongolia - an appraisal of the geodynamic development by the study of sandstone provenance and detrital zircons. Tectonophysics 510, 132–150.

Crameri, F., Magni, V., Domeier, M., Shephard, G.E., Chotalia, K., Cooper, G., Eakin, C. M., Grima, A.G., Gürer, D., Király, Á., Mulyukova, E., Peters, K., Robert, B., Thielmann, M., 2020. A transdisciplinary and community-driven database to unravel subduction zone initiation. Nat. Commun. 11, 1–14.

Davidson, J., Turner, S., Handley, H., MacPherson, C., Dosseto, A., 2007. Amphibole "sponge" in arc crust? Geology 35 (9), 787.

Donskaya, T.V., Gladkochub, D.P., Mazukabzov, A.M., Ivanov, A.V., 2013. Late Paleozoic–Mesozoic subduction – related magmatism at the southern margin of the Siberian continent and the 150 million–year history of the Mongol–Okhotsk Ocean. J. Asian Earth Sci. 62, 79–97.

Gao, S., Rudnick, R.L., Yuan, H.L., Liu, X.M., Liu, Y.S., Xu, W.L., Ling, W.L., Ayers, J., Wang, X.C., Wang, Q.H., 2004. Recycling lower continental crust in the North China craton. Nature 432 (7019), 892–897.

Griffin, W.L., Belousova, E.A., Shee, S.R., Pearson, N.J., O'Reilly, S.Y., 2004. Archean crustal evolution in the northern Yilgam Craton: U-Pb and Hf-isotope evidence from detrital zircons. Precambr. Res. 131 (3–4), 231–282.

Griffin, W.L., Pearson, N.J., Belousova, E.A., Jackson, S.E., O'Reilly, S.Y., van Achterberg, E., Shee, S.R., 2000. The Hf isotope composition of cratonic mantle: LAM-MC-ICPMS analysis of zircon megacrysts in kimberlites. Geochim. Cosmochim. Ac. 64, 133–147.

Guilmette, C., Smit, M.A., van Hinsbergen, D.J.J., Corfu, F., Gürer, D., Charette, B., Maffione, M., Rabeau, O., Savard, D., 2018. Forced subduction initiation revealed by crust-sole geochronology of the Semail ophiolite. Nat. Geosci. 11, 688–695.

Gurnis, M., Hall, C., Lavier, L., 2004. Evolving force balance during incipient subduction. Geochem. Geophys. Geosyst. 5, Q07001.

Hanyu, T., Tatsumi, Y., Nakai, S., 2002. A contribution of slab-melts to the formation of high-Mg andesite magmas; Hf isotopic evidence from SW Japan. Geophys. Res. Lett. 29 (22), 2051.

Hanyu, T., Tatsumi, Y., Nakai, S., Chang, Q., Miyazaki, T., Sato, K., Tani, K., Shibata, T., Yoshida, T., 2006. Contribution of slab melting and slab dehydration to magmatism in the ne Japan arc for the last 25 Myr: constraints from geochemistry. Geochem. Geophys. Geosyst. 7 (8).

Hickey-Vargas, R., Yogodzinski, G.M., Bizimis, M., Ishizuka, O., McCarthy, A., Kusano, Y., Savov, I.P., Arculus, R., 2018. Origin of depleted basalts during subduction ini-tiation: evidence from IODP Expedition 351 Site U1438, Amami Sankaku Basin. Geochim. Cosmochim. Acta 229, 85–111.

van Hinsbergen, D.J.J., Peters, K., Maffione, M., Spakman, W., Guilmette, C., Thieulot, C., Plümper, O., Gürer, D., Brouwer, F.M., Aldanmaz, E., Kaymakcı, N., 2015. Dynamics of intraoceanic subduction initiation: 2. Suprasubduction zone ophiolite formation and metamorphic sole exhumation in context of absolute plate motions. Geochem. Geophys. Geosyst. 16, 1771–1785.

Irvine, T.N., Baragar, W.R.A., 1971. A guide to the chemical classification of the common volcanic rocks. Can. J. Earth Sci. 8, 523–548.

Ishizuka, O., Tani, K., Reagan, M.K., Kanayama, K., Umino, S., Harigane, Y., Sakamoto, I., Miyajima, Y., Yuasa, M., Dunkley, D.J., 2011. The time scales of subduction initiation and subsequent evolution of an oceanic island arc. Earth Planet. Sci. Lett. 306, 229–240.

Ishizuka, O., Tani, K., Reagan, M.K., 2014. Izu–Bonin–Mariana forearc crust as a modern ophiolite analogue. Elements 10 (2), 115–120.

Jackson, S.E., Pearson, N.J., Griffin, W.L., Belousova, E.A., 2004. The application of laser ablation-inductively coupled plasma-mass spectrometry to in situ U-Pb zircon geochronology. Chem. Geol. 211, 47–69.

Kamei, A., Owada, M., Nagao, T., Shiraki, K., 2004. High-Mg diorites derived from sanukitic HMA magmas, Kyushu Island, Southwest Japan arc: evidence from clinopyroxene and whole rock compositions. Lithos 75, 359–371.

Karsli, O., Dokuz, A., Kandemir, R., 2017. Zircon Lu-Hf isotope systematics and U-Pb geochronology, whole-rock Sr-Nd isotopes and geochemistry of the early Jurassic Gokcedere pluton, Sakarya zone-NE Turkey: a magmatic response to roll-back of the Paleo-Tethyan oceanic lithosphere. Contrib. Mineral. Petrol. 172 (5), 31.

Kelty, T.K., Yin, A., Dash, B., Gehrels, G.E., Ribeiro, A.E., 2008. Detrital-zircon geochronology of Paleozoic sedimentary rocks in the Hangay–Hentey basin, north-central Mongolia: implications for the tectonic evolution of the Mongol–Okhotsk Ocean in central Asia. Tectonophysics 451, 290–311.

Kurihara, T., Tsukada, K., Otoh, S., Kashiwagi, K., Minjin, C.H., Dorjsuren, B., Bujinlkham, B., Sersmaa, G., Manchuk, N., Niwa, M., Tokiwa, T., Hikichi, G., Kozuka, T., 2009. Upper Silurian and Devonian pelagic deep-water radiolarian chert from the Khangai-Khentei, belt of Central Mongolia: evidence for Middle Palaeozoic subduction-accretion in the Central Asian Orogenic Belt. J. Asian Earth Sci. 34, 209–225.

Labanieh, S., Chauvel, C., Germa, A., Auidelleur, X., 2012. Martinique: a clear case for sediment melting and slab dehydration as a function of distance to the trench. J. Petrol. 53, 2441–2464.

Li, Q.L., Li, X.H., Liu, Y., Tang, G.Q., Yang, J.H., Zhu, W.G., 2010. Precise U-Pb and Pb-Pb dating of Phanerozoic baddeleyite by SIMS with oxygen flooding technique. J. Anal. Atom. Spectrom. 25, 1107–1113.

Li, X.H., Abd El-Rahman, Y., Abu Anbar, M., Li, J., Ling, X.X., Wu, L.G., Masoud, A.E., 2018. Old continental crust underlying juvenile oceanic arc: evidence from northern Arabian-Nubian Shield, Egypt. Geophys. Res. Lett. 45, 3001–3008.

Li, Y.J., Wang, G.H., Santosh, M., Wang, J.F., Dong, P.P., Li, H.Y., 2020. Subduction initiation of the SE Paleo-Asian Ocean: evidence from a well preserved intra-oceanic forearc ophiolite fragment in Central Inner Mongolia, North china. Earth Planet. Sci. Lett. 535, 116087.

Ludwig, K.R., 2003. User's manual for isoplot 3.00. In: A Geochronological Toolkit for Microsoft Excel. Berkeley Geochronology Centre, Berkeley, California, pp. 1–70 (Special Publication No. 4a).

Macpherson, C.G., Hall, R., 2001. Tectonic setting of Eocene boninite magmatism in the Izu–Bonin–Mariana forearc. Earth Planet. Sci. Lett. 186, 215–230.

McCarron, J.J., Smellie, J.L., 1998. Tectonic implications of fore-arc magmatism and generation of high-magnesian andesites: Alexander Island, Antarctica. J. Geol. Soc. London 155, 269–280.

Miao, L.C., Baatar, M., Zhang, F.Q., Anaad, C., Zhu, M.S., Yang, S.H., 2016. Cambrian Kherlen ophiolite in northeastern Mongolia and its tectonic implications: SHRIMP zircon dating and geochemical constraints. Lithos 261, 128–143.

Miao, L.C., Zhang, F.Q., Baatar, M., Zhu, M.S., Anaad, C., 2017. SHRIMP zircon U-Pb ages and tectonic implications of igneous events in the Ereendavaa metamorphic terrane in NE Mongolia. J. Asian Earth Sci. 144, 243–260.

Mitchell, A.L., Grove, T.L., 2015. Erratum to: melting the hydrous, subarc mantle: the origin of primitive andesites. Contrib. Mineral. Petrol 170.

Nakamura, K., Kato, Y., Tamaki, K., Ishii, T., 2007. Geochemistry of hydrothermally altered basaltic rocks from the Southwest Indian Ridge near the Rodriguez Triple Junction. Mar. Geol. 239, 125–141.

Narantsetseg, T., Orolmaa, D., Yuan, C., Wang, T., Guo, L., Tong, Y., Wang, X., Orshikh, O.E., Oyunchimeg, T., Delgerzaya, P., Enkhdalai, B., 2019. Early - middle Paleozoic volcanic rocks from the Ereendavaa terrane (Tsarigiin gol area, NE Mongolia) with implications for tectonic evolution of the Kherlen massif. J. Asian Earth Sci. 175, 138–157.

Niu, Y.L., 1997. Mantle melting and melt extraction processes beneath ocean ridges: evidence from abyssal peridotites. J. Petrol. 38, 1047–1074.

Orolmaa, D., Turbold, S., Odgerel, D., 2015. Lower Paleozoic granitoids of Undurkhaan district: geochronology and geochemistry. Explorer 53, 54–68.

Paton, C., Woodhead, J.D., Hellstrom, J.C., Hergt, J.M., Greig, A., Maas, R., 2010. Improved laser ablation U-Pb zircon geochronology through robust downhole fractionation correction. Geochem. Geophy. Geosy. 11, Q0AA06.

Pearce, J.A., 2008. Geochemical fingerprinting of oceanic basalts with applications to ophiolite classification and the search for Archean oceanic crust. Lithos 100 (1–4), 14–48.

Pearce, J.A., 2014. Immobile Element Fingerprinting of Ophiolites. Elements 10, 101–108.

Pilot, J., Werner, C.D., Haubrich, F., Baumann, N., 1998. Palaeozoic and Proterozoic zircons from the mid-Atlantic ridge. Nature 393, 676–679.

Qian, Q., Hermann, J., 2010. Formation of high-Mg diorites through assimilation of peridotite by monzodiorite magma at crustal depths. J. Petrol. 51, 1381–1416.

Reagan, M.K., Ishizuka, O., Stern, R.J., Kelley, K.A., Ohara, Y., Blichert-Toft, J., Bloomer, S.H., Cash, J., Fryer, P., Hanan, B., Hickey-Vargas, R., Ishii, T., Kimura, J.-I., Peate, D.W., Rowe, M.C., Woods, M., 2010. Fore-arc basalts and subduction initiation in the Izu–Bonin–Mariana system. Geochem. Geophys. Geosyst. 11, 1–17.

Ren, R., Han, B.F., Xu, Z., Zhou, Y.Z., Liu, B., Zhang, L., Chen, J.F., Su, L., Li, J., Li, X.H., Li, Q.L., 2014. When did the subduction first initiate in the southern Paleo-Asian Ocean: new constraints from a Cambrian intra-oceanic arc system in West Junggar, NW China. Earth Planet. Sci. Lett 388, 222–236.

Rollinson, H.R., 1993. Using Geochemical Data: Evaluation, Presentation, Interpretation: London. Longman Geochemistry Society 352, 184–186.

Rubatto, D., 2002. Zircon trace element geochemistry: partitioning with garnet and the link between U-Pb ages and metamorphism. Chem. Geol. 184 (1–2), 123–138.

Saccani, E., 2015. A new method of discriminating different types of post-Archean ophiolitic basalts and their tectonic significance using Th-Nb and Ce-Dy-Yb systematics. Geosci. Front. 6, 481–501.

Shao, W.Y., Chung, S.L., Chen, W.S., Lee, H.Y., Xie, L.W., 2015. Old continental zircons from a young oceanic arc, eastern Taiwan: Implications for Luzon subduction initiation and Asian accretionary orogeny. Geology 43 (6), 479–482.

Shervais, J.W., Reagan, M.K., Godard, M., Prytulak, J., Ryan, J.G., Pearce, J.A., Almeev, R.R., Li, H., Haugen, E., Chapman, T., Kurz, W., Nelson, W.R., Heaton, D.E., Kirchenbaur, M., Shimizu, K., Sakuyama, T., Vetter, S.K., Li, Y., Whattam, S., 2021. Magmatic response to subduction initiation, part II: boninites and related rocks of the Izu-Bonin arc from IOPD expedition 352. Geochem. Geophys. Geosyst. 22, e2020GC009093.

Sláma, J., Košler, J., Condon, D.J., Crowley, J.L., Gerdes, A., Hanchar, J.M., Horstwood, M.S.A., Morris, G.A., Nasdala, L., Norberg, N., Schaltegger, U., 2008. Plešovice zircon-a new natural reference material for U-Pb and Hf isotopic microanalysis. Chem. Geol. 249, 1–35.

Smithies, R.H., Champion, D.C., 2000. The Archaean high-Mg diorite suite: links to tonalite–trondhjemite–granodiorite magmatism and implications for early Archaean crustal growth. J. Petrol. 41, 1653–1671.

Sorokin, A.A., Zaika, V.A., Kovach, V.P., Kotov, A.B., Xu, W., Yang, H., 2020. Timing of closure of the eastern Mongol–Okhotsk Ocean: Constraints from U–Pb and Hf isotopic data of detrital zircons from metasediments along the Dzhagdy Transect. Gondwana Res. 81, 58–78.

Stacey, J.S., Kramers, J.D., 1975. Approximation of terrestrial lead isotope evolution by a two-stage model. Earth Planet. Sci. Lett. 26, 207–221.

Stern, R.J., 2002. Subduction zones. Rev. Geophys. 40 (4), 1012.

Stern, R.J., 2004. Subduction initiation: spontaneous and induced. Earth Planet. Sci. Lett. 226, 275–292.

Stern, R.J., Gerya, T., 2018. Subduction initiation in nature and models: a review. Tectonophysics 746, 173–198.

Straub, S.M., Gomez-Tuena, A., Stuart, F.M., Zellmer, G.F., Espinasa-Perena, R., Cai, Y., Iizuka, Y., 2011. Formation of hybrid arc andesites beneath thick continental crust. Earth Planet. Sci. Lett. 303, 337–347.

Sun, D.Y., Gou, J., Wang, T.H., Ren, Y.S., Liu, Y.J., Guo, H.Y., Liu, X.M., Hu, Z.C., 2013. Geochronological and geochemical constraints on the Erguna massif basement, NE China – subduction history of the Mongol–Okhotsk oceanic crust. Int. Geol. Rev. 55, 1801–1816.

Sun, S.S., McDonough, W.F., 1989. Chemical and isotopic systematics of oceanic basalts; implications for mantle composition and processes. In: Saunders, A.D., Norry, M.J. (Eds.), Magmatism in the Ocean Basins, vol. 42. Geological Society Special Publications, pp. 313–345.

Tapster, S., Roberts, N.M.W., Petterson, M.G., Saunders, A.D., Naden, J., 2014. From continent to intra-oceanic arc: Zircon xenocrysts record the crustal evolution of the Solomon island arc. Geology 42, 1087–1090.

Tatsumi, Y., 2001. Geochemical modeling of partial melting of subducting sediments and subsequentmelt-mantle interaction: generation of high-Mg andesites in the Setouchi volcanic belt, Southwest Japan. Geology 29 (4), 323–326.

Tatsumi, Y., 2006. High-Mg andesites in the Setouchi volcanic belt, southwestern Japan: analogy to Archean magmatism and continental crust formation? Annu. Rev. Earth Planet. Sci. 34, 467–499.

Tomurtogoo, O., Windley, B.F., Kroner, A., Badarch, G., Liu, D.Y., 2005. Zircon age and occurrence of the Adaatsag ophiolite and Muron shear zone, central Mongolia: constraints on the evolution of the Mongol–Okhotsk ocean, suture and orogen. J. Geol. Soc. 162, 125–134.

Van der Voo, R., van Hinsbergen, D.J., Domeier, M., Spakman, W., Torsvik, T.H., 2015. Latest Jurassic - earliest Cretaceous closure of the Mongol–Okhotsk Ocean: a paleomagnetic and seismological-tomographic analysis. Geol. Soc. Am. Spec. Pap. 513, 589–606.

Whattam, S.A., Stern, R.J., 2011. The 'subduction initiation rule': a key for linking ophiolites, intra-oceanic forearcs, and subduction initiation. Contrib. Mineral. Petrol. 162 (5), 1031–1045.

Wiedenbeck, M., Alle, P., Corfu, F., Griffin, W.L., Oberli, F., Von, Q.A., Roddick, J.C., Spiegel, W., 1995. Three natural zircon standards for U–Th–Pb, Lu- Hf, trace element and REE analyses. Geostand. Newslett. 19, 1–23.

Winchester, J.A., Floyd, P.A., 1977. Geochemical discrimination of different magma series and their differentiation products using immobile elements. Chem. Geol. 20, 325–343.

Windley, B.F., Alexeiev, D., Xiao, W., Kroner, A., Badarch, G., 2007. Tectonic models for accretion of the Central Asian Orogenic Belt. J. Geol. Soc. 164, 31–47.

Woodhead, J.D., Hergt, J.M., Davidson, J.P., Eggins, S.M., 2001. Hafnium isotope evidence for 'conservative' element mobility during subduction zone processes. Earth Planet. Sci. Lett. 192 (3), 331e346.

Wu, F.Y., Sun, D.Y., Ge, W.C., Zhang, Y.B., Grant, M.L., Wilde, S.A., Jahn, B.M., 2011. Geochronology of the Phanerozoic granitoids in northeastern China. J. Asian Earth Sci. 41, 1–30.

Wu, F.Y., Yang, Y.H., Xie, L.W., Yang, J.H., Xu, P., 2006. Hf isotopic compositions of the standard zircons and baddeleyites used in U-Pb geochronology. Chem. Geol. 234 (1), 105–126.

Xiao, W., Windley, B.F., Sun, S., Li, J., Huang, B., Han, C., Yuan, C., Sun, M., Chen, H., 2015. A Tale of Amalgamation of three Permo-Triassic Collage Systems in Central Asia: Oroclines, Sutures, and Terminal Accretion. Annu. Rev. Earth Planet. Sci. 43, 477–507.

Yi, Z.Y., Meert, J.G., 2020. A closure of the Mongol-Okhotsk ocean by the middle jurassic: reconciliation of paleomagnetic and geological evidence. Geophys. Res. Lett. 47, e2020GL088235.

Zeng, Y., Chen, J., Xu, J., Wang, B., Huang, F., 2016. Sediment melting during subduction initiation: geochronological and geochemical evidence fromthe Darutso high-Mg andesites within ophiolite melange, Central Tibet. Geochem. Geophys. Geosyst. 17 (12), 4859–4877.

Zhao, C., Qin, K.Z., Song, G.X., Li, G.M., 2019. Switch of geodynamic setting from the Paleo-Asian Ocean to the Mongol-Okhotsk Ocean: evidence from granitoids in the Duobaoshan ore field, Heilongjiang Province, Northeast China. Lithos 336, 202–220.

Zhao, P., Xu, B., Jahn, B.M., 2017. The Mongol-Okhotsk Ocean subduction-related Permian peraluminous granites in northeastern Mongolia: constraints from zircon U-Pb ages, whole-rock elemental and Sr-Nd-Hf isotopic compositions. J. Asian Earth Sci. 144, 225–242.

Zhu, M.S., Zhang, F.Q., Miao, L.C., Baatar, M., Anaad, C., Yang, S.H., Li, X.B., 2018. The Late Carboniferous Khuhu Davaa ophiolite in northeastern Mongolia: Implications for the tectonic evolution of the Mongol–Okhotsk Ocean. Geol. J. 53, 1263–1278.

Zhu, M.S., Miao, L.C., Zhang, F.Q., Ganbat, A., Baatar, M., Anaad, C., Yang, S.H., Wang, Z.L., 2022. Carboniferous magmatic records of central Mongolia and its implications for the southward subduction of the Mongol–Okhotsk Ocean. Int. Geol. Rev. https://doi.org/10.1080/00206814.2022.2076161.

Zorin, Y.A., 1999. Geodynamics of the western part of the Mongolia–Okhotsk collisional belt, Trans-Baikal region (Russia) and Mongolia. Tectonophysics 306, 33–56.